

Durham Research Online

Deposited in DRO:

17 January 2019

Version of attached file:

Published Version

Peer-review status of attached file:

Peer-reviewed

Citation for published item:

Ichikawa, Kohei and Ricci, Claudio and Ueda, Yoshihiro and Bauer, Franz E. and Kawamuro, Taiki and Koss, Michael J. and Oh, Kyuseok and Rosario, David J. and Shimizu, T. Taro and Stalevski, Marko and Fuller, Lindsay and Packham, Christopher and Trakhtenbrot, Benny (2019) 'BAT AGN Spectroscopic Survey. XI. The covering factor of dust and gas in swift/BAT active galactic nuclei.', *Astrophysical journal.*, 870 (1). p. 31.

Further information on publisher's website:

<https://doi.org/10.3847/1538-4357/aaef8f>

Publisher's copyright statement:

© 2019. The American Astronomical Society. All rights reserved.

Additional information:

Use policy

The full-text may be used and/or reproduced, and given to third parties in any format or medium, without prior permission or charge, for personal research or study, educational, or not-for-profit purposes provided that:

- a full bibliographic reference is made to the original source
- a [link](#) is made to the metadata record in DRO
- the full-text is not changed in any way

The full-text must not be sold in any format or medium without the formal permission of the copyright holders.

Please consult the [full DRO policy](#) for further details.



BAT AGN Spectroscopic Survey. XI. The Covering Factor of Dust and Gas in *Swift*/BAT Active Galactic Nuclei

Kohei Ichikawa^{1,2,3,4} , Claudio Ricci^{5,6,7} , Yoshihiro Ueda⁸ , Franz E. Bauer^{9,10} , Taiki Kawamuro^{11,19} , Michael J. Koss¹² , Kyuseok Oh^{8,19} , David J. Rosario¹³ , T. Taro Shimizu¹⁴ , Marko Stalevski^{15,16} , Lindsay Fuller², Christopher Packham^{2,11}, and Benny Trakhtenbrot^{17,18}

¹ Department of Astronomy, Columbia University, 550 West 120th Street, New York, NY 10027, USA; k.ichikawa@astr.tohoku.ac.jp

² Department of Physics and Astronomy, University of Texas at San Antonio, One UTSA Circle, San Antonio, TX 78249, USA

³ Frontier Research Institute for Interdisciplinary Sciences, Tohoku University, Sendai, Miyagi 980-8578, Japan

⁴ Astronomical Institute, Tohoku University, Aramaki, Aoba-ku, Sendai, Miyagi 980-8578, Japan

⁵ Núcleo de Astronomía de la Facultad de Ingeniería, Universidad Diego Portales, Av. Ejército Libertador 441, Santiago, Chile

⁶ Kavli Institute for Astronomy and Astrophysics, Peking University, Beijing 100871, People's Republic of China

⁷ Chinese Academy of Sciences South America Center for Astronomy, Camino El Observatorio 1515, Las Condes, Santiago, Chile

⁸ Department of Astronomy, Kyoto University, Oiwake-cho, Sakyo-ku, Kyoto 606-8502, Japan

⁹ Millennium Institute of Astrophysics (MAS), Nuncio Monseñor Sótero Sanz 100, Providencia, Santiago, Chile

¹⁰ Space Science Institute, 4750 Walnut Street, Suite 205, Boulder, CO 80301, USA

¹¹ National Astronomical Observatory of Japan, 2-21-1 Osawa, Mitaka, Tokyo 181-8588, Japan

¹² Eureka Scientific, 2452 Delmer Street Suite 100, Oakland, CA 94602-3017, USA

¹³ Centre for Extragalactic Astronomy, Department of Physics, Durham University, South Road, DH1 3LE Durham, UK

¹⁴ Max-Planck-Institut für extraterrestrische Physik, Postfach 1312, D-85741, Garching, Germany

¹⁵ Astronomical Observatory, Volgina 7, 11060 Belgrade, Serbia

¹⁶ Sterrenkundig Observatorium, Universiteit Gent, Krijgslaan 281-S9, Gent B-9000, Belgium

¹⁷ Department of Physics, ETH Zurich, Wolfgang-Pauli-Strasse 27, CH-8093 Zurich, Switzerland

¹⁸ School of Physics and Astronomy, Tel Aviv University, Tel Aviv 69978, Israel

Received 2018 March 7; revised 2018 October 12; accepted 2018 November 2; published 2019 January 2

Abstract

We quantify the luminosity contribution of active galactic nuclei (AGNs) to the 12 μm , mid-infrared (MIR; 5–38 μm), and total IR (5–1000 μm) emission in the local AGNs detected in the all-sky 70 month *Swift*/Burst Alert Telescope (BAT) ultrahard X-ray survey. We decompose the IR spectral energy distributions (SEDs) of 587 objects into the AGN and starburst components using templates for an AGN torus and a star-forming galaxy. This enables us to recover the emission from the AGN torus including the low-luminosity end, down to $\log(L_{14-150}/\text{erg s}^{-1}) \simeq 41$, which typically has significant host galaxy contamination. The sample demonstrates that the luminosity contribution of the AGN to the 12 μm , the MIR, and the total IR bands is an increasing function of the 14–150 keV luminosity. We also find that for the most extreme cases, the IR pure-AGN emission from the torus can extend up to 90 μm . The total IR AGN luminosity obtained through the IR SED decomposition enables us to estimate the fraction of the sky obscured by dust, i.e., the dust covering factor. We demonstrate that the median dust covering factor is always smaller than the median X-ray obscuration fraction above an AGN bolometric luminosity of $\log(L_{\text{bol}}^{(\text{AGN})}/\text{erg s}^{-1}) \simeq 42.5$. Considering that the X-ray obscuration fraction is equivalent to the covering factor coming from both the dust and gas, this indicates that an additional neutral gas component, along with the dusty torus, is responsible for the absorption of X-ray emission.

Key words: galaxies: active – galaxies: nuclei – infrared: galaxies

Supporting material: figure set, machine-readable table

1. Introduction

One of the fundamental open questions of extragalactic astrophysics is how supermassive black holes (SMBHs) and their host galaxies coevolve (e.g., Alexander & Hickox 2012). Active galactic nuclei (AGNs) are the best targets for understanding this process of coevolution, because they are in the stage where mass accretion onto SMBHs occurs with the release of large amounts of radiation (e.g., Yu & Tremaine 2002; Marconi et al. 2004), until they reach their maximum achievable mass of $M_{\text{BH}} \simeq 10^{10.5} M_{\odot}$ (Netzer 2003; McLure & Dunlop 2004; Trakhtenbrot 2014; Jun et al. 2015; Inayoshi & Haiman 2016; Ichikawa & Inayoshi 2017).

Ultrahard ($E > 10$ keV) X-ray observations are one of the most reliable methods for identifying AGNs. Thanks to the

combination of (1) a strong penetration power up to $\log(N_{\text{H}}/\text{cm}^{-2}) \simeq 24$ (e.g., Ricci et al. 2015) and (2) the high contrast with stellar X-ray emission (e.g., Mineo et al. 2012), ultrahard X-ray surveys allow an unbiased census of AGNs up to Compton-thick levels (e.g., Koss et al. 2016). Among the recent available surveys, *Swift*/BAT provides the most sensitive X-ray survey of the whole sky in the 14–195 keV range, reaching a flux level of $(1.0\text{--}1.3) \times 10^{-11} \text{ erg s}^{-1} \text{ cm}^{-2}$ in the first 70 months of operations (Baumgartner et al. 2013), and a deeper flux of $(7.2\text{--}8.4) \times 10^{-12} \text{ erg s}^{-1} \text{ cm}^{-2}$ in the recently updated 105 month catalog (Oh et al. 2018).

Infrared (IR) observations also provide an effective method to study AGNs because the central engine of an AGN is expected to be surrounded by a dusty “torus” (Krolik & Begelman 1986), which is heated by the AGN and re-emits thermally in the mid-IR (MIR) (e.g., Gandhi et al. 2009;

¹⁹ JSPS fellow.

Ichikawa et al. 2012, 2017; Asmus et al. 2015). A recent upward revision of black hole scaling relations (Kormendy & Ho 2013) indicates that the local mass density in black holes should be higher, suggesting that a larger population of heavily obscured AGN gas and dust is required to fill the mass gap of the revised local black hole mass density (e.g., Novak 2013; Comastri et al. 2015). These populations contribute significantly to the infrared background (e.g., Murphy et al. 2011; Delvecchio et al. 2014), especially in the MIR band (Risaliti et al. 2002). However, since star formation from the host galaxy sometimes contaminates the MIR emission, especially for low-luminosity AGNs with $L_{14-150} < 10^{43}$ erg s $^{-1}$ (e.g., Ichikawa et al. 2017), and the torus is too compact (< 10 pc; e.g., Jaffe et al. 2004) to be fully resolved (e.g., García-Burillo et al. 2016; Imanishi et al. 2018), the precise estimation of AGN thermal activity is not straightforward.

Fortunately, several methods have been proposed to isolate the emission from the torus from the starburst component. One of them is to use MIR observations with high spatial resolution ($\sim 0''.3-0''.7$) to resolve the starburst emission of the host galaxies down to scales of 10 pc (Packham et al. 2005; Radomski et al. 2008; Hönig et al. 2010; Alonso-Herrero et al. 2011, 2016; Ramos Almeida et al. 2011; González-Martín et al. 2013; Asmus et al. 2014; Ichikawa et al. 2015; Martínez-Paredes et al. 2017). In addition, the advent of IR interferometric observations, with their exquisite resolving power (with baselines up to 130 m), has spatially resolved the dusty nuclear regions and shown that their outer radii in the MIR are typically several parsecs (e.g., Jaffe et al. 2004; Raban et al. 2009; Bartscher et al. 2013). Notably, some show the polar elongated dust emission suggestive of a dusty outflow (Hönig et al. 2012, 2013; Tristram et al. 2014; López-Gonzaga et al. 2016, Leftley et al. 2018). However, because of the limited sensitivity and the spatial resolution of current telescopes (see a recent review by Bartscher et al. 2016), these two methods are available only for a few tens of bright sources located in the very local universe ($z < 0.01$). Another possible approach is to separate the spectral emission of the AGN and the starburst (SB) component. Multiple decomposition methods have been applied to MIR spectra, mainly using aromatic features as a proxy for star formation (e.g., Tran et al. 2001; Lutz et al. 2004; Sajina et al. 2007; Alonso-Herrero et al. 2012; Ichikawa et al. 2014; Hernán-Caballero et al. 2015; Kirkpatrick et al. 2015; Symeonidis et al. 2016), to broadband IR spectral energy distributions (SEDs, e.g., da Cunha et al. 2008; Hatziminaoglou et al. 2008; Xu et al. 2015; Lyu et al. 2016, 2017; Shimizu et al. 2017), and to the combination of both spectra and SEDs (e.g., Mullaney et al. 2011). The advantage of the SED decomposition is that it is less affected by the differing spatial resolutions inherent in aperture photometry, and can be applied to high- z sources (e.g., Stanley et al. 2015; Lyu et al. 2016; Mateos et al. 2016) and/or to large ($N > 100$) samples, for which MIR imaging and spectroscopy with high spatial resolution would require significant amounts of time on large-diameter (> 8 m) telescopes.

In this paper, we decompose the IR SEDs of the ultrahard X-ray-selected *Swift*/BAT 70 month AGN catalog (Baumgartner et al. 2013) into AGN and host galaxy components. Thanks to intensive follow-up observations by BAT AGN Spectroscopic Survey²⁰ (BASS; Koss et al. 2017; Lamperti et al. 2017;

Ricci et al. 2017b), we are able to obtain reliable information on the gas column density (N_{H}), absorption-corrected 14–150 keV X-ray luminosity, and black hole mass (M_{BH}) of the sample.

The main goal of this work is to quantitatively assess the AGN contribution to the 12 μm band, MIR (5–38 μm) band, and total IR (5–1000 μm) band down to $\log(L_{14-150}/\text{erg s}^{-1}) \simeq 41$ in order to investigate torus (1) the correlation between MIR and X-ray luminosity and (2) the dust covering factor of the torus, minimizing issues related to host galaxy contamination. Throughout the paper, we adopt standard cosmological parameters ($H_0 = 70.0$ km s $^{-1}$ Mpc $^{-1}$, $\Omega_{\text{M}} = 0.3$, and $\Omega_{\Lambda} = 0.7$).

2. Sample

Our initial sample is based on the sample of Ichikawa et al. (2017), which contains the 606 non-blazar AGNs from the *Swift*/BAT 70 month catalog (Baumgartner et al. 2013) at galactic latitudes ($|b| > 10^\circ$) for which secure spectroscopic redshifts are available. In this study, we use the column density (N_{H}) and the absorption-corrected 14–150 keV luminosity (L_{14-150}) tabulated in Ricci et al. (2017b). They are also summarized in Table 1.

In Ichikawa et al. (2017), we reported the 3–500 μm IR counterparts for our AGN sample, utilizing the IR catalogs obtained from *WISE* (Wright et al. 2010; Cutri et al. 2013), *AKARI* (Murakami et al. 2007), *IRAS* (Beichman et al. 1988), and *Herschel* (Griffin et al. 2010; Poglitsch et al. 2010). Out of the 606 sources, we identified 604, 560, 601, and 402 counterparts in the total IR, near-IR (NIR; $< 5 \mu\text{m}$), MIR, and far-IR (FIR; 60–500 μm) bands, respectively. The reader should refer to Ichikawa et al. (2017) for details of the IR catalogs. While Ichikawa et al. (2017) compiled the representative fluxes at 12, 22, 70, and 90 μm , by combining similar wavelength bands in the multiple IR catalogs listed above, in this study we regard each IR band with a different central wavelength as independent photometry. Therefore, there are at most 17 available IR photometric bands between 3 and 500 μm , as identified in Table 1. For the data points with the same wavelengths (i.e., 12, 25, 60, 100, and 160 μm), the adopted photometry was chosen based on the priorities reported in the IR catalog of Ichikawa et al. (2017) to measure the IR emission from both nucleus and host galaxy in a uniform way for the entire AGN sample. The 12 μm flux density was obtained with the following priority: *WISE*, *IRAS*/Point Source Catalog (PSC), and *IRAS*/Faint Source Catalog (FSC). For the 25, 60, and 100 μm flux densities, on the other hand, we followed a different order (*IRAS*/PSC and *IRAS*/FSC), while for the 160 μm flux density we used *Herschel*/PACS and, when not available, *AKARI*/FIS. The corrected data are obtained from a wide range of different angular resolutions from *Herschel*/PACS (70 μm ; 6 arcsec) to *IRAS*/FIR (100 μm ; ≈ 1 arcmin). Using nearly the same sample, Mushotzky et al. (2014) already showed that the bulk of PACS 70 μm is point-like at the spatial resolution of *Herschel*, suggesting that the FIR emission from the host galaxy is really compact (with a median value of 2 kpc FWHM) and unresolvable for most of our sample. Thus, we conclude that the aperture dependence with more moderate resolutions obtained by *AKARI* and *IRAS* is negligible (see also Meléndez et al. 2014; García-González et al. 2016a; Ichikawa et al. 2017; Lutz et al. 2018).

²⁰ www.bass-survey.com

Table 1
Column Descriptions for the IR Catalog of the *Swift*/BAT 70 Month AGN Survey

Col. #	Header Name	Format	Unit	Description
1	objID	string	...	<i>Swift</i> /BAT ID as shown in Baumgartner et al. (2013)
2	ctpt1	string	...	optical counterpart name
3	z	float	...	redshift
4	NH_log	float	...	logarithmic column density ($\log(N_{\text{H}}/\text{cm}^{-2})$)
5	lbat_log	float	...	absorption-corrected logarithmic 14–150 keV luminosity ($\log(L_{14-150}/\text{erg s}^{-1})$)
6	lbol_const_log	float	...	logarithmic bolometric AGN luminosity ($\log(L_{\text{bol}}^{(\text{AGN})}/\text{erg s}^{-1})$)
7	lbol_log	float	...	logarithmic bolometric AGN luminosity ($\log(L_{\text{bol}}^{(\text{M04})}/\text{erg s}^{-1})$) using Marconi et al. (2004)
8 (9)	fnu3p4_(err)_fqualmod	float	Jy	3.4 μm profile-fitting flux density (error) obtained from <i>WISE</i>
10 (11)	fnu4p6_(err)_fqualmod	float	Jy	4.6 μm profile-fitting flux density (error) obtained from <i>WISE</i>
12 (13)	fnu9a_(err)_fqualmod	float	Jy	9.0 μm flux density (error) obtained from <i>AKARI</i> /IRC
14 (15)	fnu12wipf_(err)_fqualmod	float	Jy	12 μm flux density (error)
16	fnu12wipcatalog	string	...	reference catalogs for 12 μm : W = <i>WISE</i> , Ip = <i>IRAS</i> /PSC, If = <i>IRAS</i> /FSC
17 (18)	fnu18a_(err)_fqualmod	float	Jy	18.0 μm flux density (error) obtained from <i>AKARI</i>
19 (20)	fnu22w_(err)_fqualmod	float	Jy	22 μm profile-fitting flux density (error) obtained from <i>WISE</i>
21 (22)	fnu25ipf_(err)_fqualmod	float	Jy	25 μm flux density (error)
23	fnu25ipfcatalog	string	...	reference catalogs for 25 μm : Ip = <i>IRAS</i> /PSC, If = <i>IRAS</i> /FSC
24 (25)	fnu60ipf_(err)_fqualmod	float	Jy	60 μm flux density (error)
26	fnu60ipfcatalog	string	...	reference catalogs for 60 μm : Ip = <i>IRAS</i> /PSC, If = <i>IRAS</i> /FSC
27 (28)	fnu65a_(err)_fqualmod	float	Jy	65 μm flux density (error) obtained from <i>AKARI</i> /FIS
29 (30)	fnu70p_(err)_fqualmod	float	Jy	70 μm flux density (error) obtained from <i>Herschel</i> /PACS
31 (32)	fnu90a_(err)_fqualmod	float	Jy	90 μm flux density (error) obtained from <i>AKARI</i> /FIS
33 (34)	fnu100ipf_(err)_fqualmod	float	Jy	100 μm flux density (error)
35	fnu100ipfcatalog	string	...	reference catalogs for 100 μm : Ip = <i>IRAS</i> /PSC, If = <i>IRAS</i> /FSC
36 (37)	fnu140a_(err)_fqualmod	float	Jy	140 μm flux density (error) obtained from <i>AKARI</i> /FIS
38 (39)	fnu160pa_(err)_fqualmod	float	Jy	160 μm flux density (error)
40	fnu160pacatalog	string	...	reference catalogs for 160 μm : P = <i>Herschel</i> /PACS, A = <i>AKARI</i> /FIS
41 (42)	fnu250s_(err)_fqualmod	float	Jy	250 μm flux density (error) obtained from <i>Herschel</i> /SPIRE
43 (44)	fnu350s_(err)_fqualmod	float	Jy	350 μm flux density (error) obtained from <i>Herschel</i> /SPIRE
45 (46)	fnu500s_(err)_fqualmod	float	Jy	500 μm flux density (error) obtained from <i>Herschel</i> /SPIRE
47	l12_AGN_afSta15_log	float	...	logarithmic decomposed 12 μm AGN luminosity $\log(L_{12\mu\text{m}}^{(\text{AGN})}/\text{erg s}^{-1})$
48	lMIR_AGN_afSta15_log	float	...	logarithmic decomposed MIR AGN luminosity $\log(L_{\text{MIR}}^{(\text{AGN})}/\text{erg s}^{-1})$
49	lIR_AGN_afSta15_log	float	...	logarithmic decomposed total IR luminosity $\log(L_{\text{IR}}^{(\text{AGN})}/\text{erg s}^{-1})$
50	l12AGNratio_afSta15	float	...	$f_{\text{AGN}}^{(12\mu\text{m})}$
51	AGNpercentage_MIR_afSta15	float	...	$f_{\text{AGN}}^{(\text{MIR})}$
52	AGNpercentage_afSta15	float	...	$f_{\text{AGN}}^{(\text{IR})}$
53	flag_upperlimit	int	...	flag of AGN: detection (= 0), upper limit (= 1), and lower-limit (= -1)
54	R_Sta16_afSta15_log	float	...	$\log R = \log(L_{\text{IR}}^{(\text{AGN})}/L_{\text{bol}}^{(\text{AGN})})$
55	CF_Sta16_tau9p7eq3_afSta15	float	...	$C_{\text{T}}(\text{dust})$
56	SBtemplate_afSta15	string	...	SB template used for the SED fitting this study: SB1–SB5

Note. The detail of the selection of the flux is compiled in Section 2. The full catalog is available as a machine readable electronic table.

(This table is available in its entirety in machine-readable form.)

To acquire IR SEDs with a number of data points sufficient for spectral decomposition we require, for each source, at least three photometric bands within the rest-frame 3–500 μm . This is because three data points are needed to define the normalization of the two components (AGN torus and host galaxy). Applying this criterion, our sample is reduced to 588 sources. In addition, we require at least one data point from either the NIR or FIR band to estimate the host galaxy component, which brings the sample to 587 sources. This is the final sample used for this study, and it represents a large fraction of the initial sample (587/606 = 97%). The redshift distribution of the sample is shown in Figure 1.²¹

We divide the sample into two AGN types based on N_{H} obtained by Ricci et al. (2017b). We define the AGNs with $N_{\text{H}} < 10^{22} \text{ cm}^{-2}$ as unobscured AGNs, and those with $N_{\text{H}} \geq 10^{22} \text{ cm}^{-2}$ as obscured ones. Overall we have 300 unobscured and 287 obscured AGNs. The AGN types for the complete BAT 70 month catalog are tabulated in Ricci et al. (2017b), as well as in Table 1. We note that Koss et al. (2017) found a 95% agreement for the unobscured and obscured AGNs with the presence of a broad H β line for optical types Seyfert 1–1.8 and Seyfert 2.

3. Analysis

We decompose the IR SEDs of AGNs using SB and AGN templates to estimate the intrinsic AGN IR luminosity. We use the IDL script `DecompIR` coded by Mullaney et al. (2011) and

²¹ M81 is not shown in the figure due to its very low redshift of $z = 10^{-4}$ (Ricci et al. 2017b).

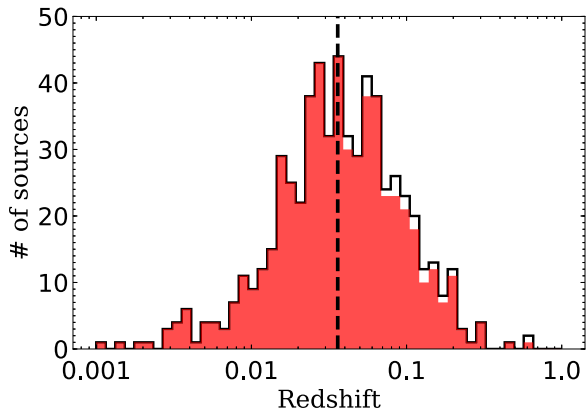


Figure 1. Redshift distribution of AGNs in the *Swift*/BAT 70 month catalog at Galactic latitude of $|b| > 10^\circ$ (black solid line: 606 objects; see also Ichikawa et al. 2017) and of those used in this study (red area: 587 objects). The vertical dashed line represents the median redshift ($\langle z \rangle = 0.037$) in our sample.

further developed by Del Moro et al. (2013). This code accepts IR photometry points in the 3–500 μm range as input and properly accounts for the filter and instrument response functions of the photometry points. It then computes the approximate levels of AGN and host galaxy contributions by fitting data that combine a host galaxy component with an AGN. *DecompIR* contains the mean AGN template produced from the *Swift*/BAT 9 month catalog (Tueller et al. 2008), which broadly traces the typical spectral forms of face-on and edge-on clumpy torus models (e.g., Nenkova et al. 2008a, 2008b) as shown in Mullaney et al. (2011). It also includes the five star-forming galaxy templates (Mullaney et al. 2011; Del Moro et al. 2013), using the average starburst SEDs derived by Dale et al. (2001). The five galaxy templates are composites of local star-forming galaxies with $L_{\text{IR}} < 10^{12} L_\odot$ (Brandl et al. 2006). They characterize well the full range of host galaxy SED shapes (Del Moro et al. 2013; Stanley et al. 2015), such as the galaxy template library of Chary & Elbaz (2001). Using these representative templates, we are able to fit the data without suffering from the degeneracy of the fitting procedure caused by the large number of templates. In addition, some of our sources have only three data points, so it is reasonable to keep the number of free parameters as small as possible.

The free parameters of the fitting are the normalizations of the AGN and host galaxy templates; therefore at least three IR data points are needed to fit the SEDs. However, we added one more free parameter for only the very luminous sources. It is known that, in high-luminosity AGNs, the IR SEDs become much flatter at shorter wavelengths, which could be related to the stronger radiation field heating the surrounding dust to higher temperatures than in moderate-luminosity AGNs (e.g., Richards et al. 2006; Netzer et al. 2007; Mullaney et al. 2011; Symeonidis et al. 2016; Lani et al. 2017; Lyu et al. 2017). Our AGN SEDs also show such a tendency, especially at high luminosities ($L_{14-150} > 10^{44} \text{ erg s}^{-1}$). Therefore, for the sources that have at least four data points and luminosities $L_{14-150} > 10^{44} \text{ erg s}^{-1}$, we also allow the spectral index α_1 of the AGN template (see Mullaney et al. 2011) to be shallower at wavelengths shorter than 19 μm .

To determine the best fitting parameters, we first fit the SED by using the five host galaxy templates (SB1–SB5) and the AGN template. We then check the results obtained using the five different SB templates, and we choose the one that

provides the best results according to the chi-squared statistic (χ^2) minimization.

Figure 2 shows examples of the best-fitting SEDs that include both the AGN and star formation components, together with the best-fitting SEDs that require only the host galaxy or the AGN component. All the other SEDs of our sample are compiled in the online journal. Overall, 474 sources required both the AGN and the host galaxy templates, while 94 sources required only the AGN template. For the latter objects, the fitting quality does not improve even when including an additional SB template. Since most of those sources (89 out of 94) are not detected in the FIR bands, and considering that the FIR bands have shallower sensitivities than the MIR ones, the lack of a significant contribution of the SB template in the MIR does not always imply that the host galaxy does not contribute to the total IR luminosity. In order to assess how much the host galaxy could contribute to the total infrared luminosity without affecting the observed SEDs, we calculate the upper limits on the contribution from star formation by following Stanley et al. (2015), where the same SED decomposition routine, *DecompIR*, was used. This was done by increasing the normalization of the host galaxy template until it reached one of the upper limits or exceeded the 3σ uncertainty of a data point. We then used the star-forming galaxy template that gave the highest value of IR luminosity as our conservative upper limit. For the sources that have an upper limit on the host galaxy component, we show the lower limits of the AGN contribution to the MIR flux (5–38 μm ; $f_{\text{AGN}}^{\text{(MIR)}}$) and to the total IR flux (5–1000 μm ; $f_{\text{AGN}}^{\text{(IR)}}$) in each SED, as illustrated in the middle panel of Figure 2. The lower limits on $f_{\text{AGN}}^{\text{(MIR)}}$ and $f_{\text{AGN}}^{\text{(IR)}}$ are reported in Table 1, and readers can use the flag (*flag_limit*) to assess whether the values are lower limits or not.

There are 18 sources in our sample that were best fit to the host galaxy template alone ($f_{\text{AGN}}^{\text{(MIR)}} = 0$). Again, in order to assess the contribution of AGNs to the total IR luminosity, we calculate the upper limits on the contribution from the AGN torus with the same methods as for the AGN-dominated SEDs, as discussed above. The upper limits of $f_{\text{AGN}}^{\text{(MIR)}}$ and $f_{\text{AGN}}^{\text{(IR)}}$ are also shown in the right panel of Figure 2 (see also Table 1).

Using this SED fitting approach, we have measurements of the AGN luminosity in the 12 μm ($L_{12\mu\text{m}}^{\text{(AGN)}}$), MIR ($L_{\text{MIR}}^{\text{(AGN)}}$), and total IR ($L_{\text{IR}}^{\text{(AGN)}}$) bands. All the values, as well as the IR flux densities, are tabulated in Table 1. We do not compile the IR star-forming luminosity, due to the impossibility of obtaining reliable estimates for the sources not detected in the FIR.

4. Results and Discussion

4.1. Fractional Luminosity Contribution of AGNs to the IR Band

Figure 3 shows the median of the AGN contributions to the 12 μm , MIR, and total IR luminosities as a function of L_{14-150} . The AGN contribution is calculated from the ratio of the AGN luminosity to the total (SF plus AGN) luminosity:

$$f_{\text{AGN}}^{(12\mu\text{m}, \text{MIR}, \text{IR})} = L_{12\mu\text{m}, \text{MIR}, \text{IR}}^{\text{(AGN)}} / (L_{12\mu\text{m}, \text{MIR}, \text{IR}}^{\text{(AGN)}} + L_{12\mu\text{m}, \text{MIR}, \text{IR}}^{\text{(SF)}}). \quad (1)$$

Figure 3 shows that the luminosity contribution of the AGNs to the 12 μm , MIR, and total IR bands increases with L_{14-195} . At the low-luminosity end ($L_{14-195} < 10^{43} \text{ erg s}^{-1}$), Figure 3 indicates that the host galaxy emission significantly

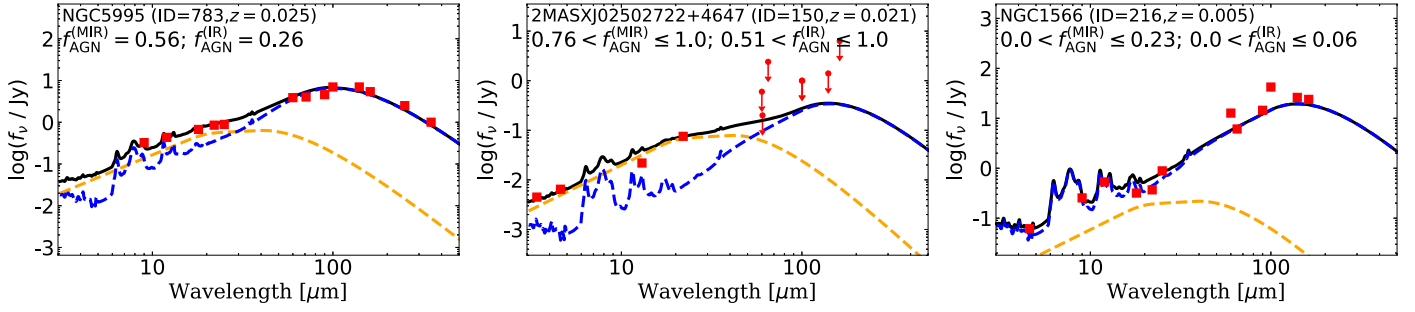


Figure 2. Example of our IR SEDs and their best-fit models. The orange and blue dashed curves represent fitted the AGN and host galaxy templates, respectively. The black solid curve is the combination of AGN and host galaxy templates, while the red squares with error bars are the flux densities. Each panel also shows the object ID based on the *Swift*/BAT 70 month catalog, the redshift, and the luminosity contribution of the AGNs to the MIR ($f_{\text{AGN}}^{(\text{MIR})}$) and IR bands ($f_{\text{AGN}}^{(\text{IR})}$). Left panel: an example of a source showing both AGN and host galaxy contributions. Middle panel: an example of an AGN torus-dominated SED. The host galaxy template is plotted as an upper limit. Right panel: an example of a source with a host galaxy-dominated SED, with the AGN template plotted as an upper limit. The complete figure set of all SEDs of our sample (587 images) is available in the online journal.

(The complete figure set (587 images) is available.)

contaminates ($\approx 50\%$ – 80%) the $12\ \mu\text{m}$ and MIR bands. At the high-luminosity end ($L_{14-195} > 10^{43}\ \text{erg s}^{-1}$), it clearly shows that the AGN component is the dominant ($\gtrsim 80\%$) energy source at $12\ \mu\text{m}$ and in the MIR band. This overall result is broadly consistent with previous studies that explored the AGN contribution using imaging with high spatial resolution (e.g., Asmus et al. 2011, 2014, and references therein). These works are discussed in Appendix A.1. On the other hand, in the total IR band, the AGN component contributes only up to $\approx 50\%$ even at high luminosities. This result is consistent with the calculations done for local quasars (Lyu et al. 2017), where it is shown that AGNs contribute $\approx 50\%$ of the flux even if they provide 90% of the MIR emission.

Figure 3 also shows that the scatter of the percentage is $\sim 20\%$ for $f_{\text{AGN}}^{(\text{MIR})}$ and increases up to $\sim 35\%$ for $f_{\text{AGN}}^{(\text{IR})}$. The scatter is mostly due to AGN-dominated sources without any detections in the FIR bands. Since no distant sources with $z > 0.05$ have been observed with *Herschel* (see Meléndez et al. 2014; Shimizu et al. 2016), those sources have very shallow upper limits: 0.2 Jy at $60\ \mu\text{m}$ (*IRAS*/FSC) and/or 0.55 Jy at $90\ \mu\text{m}$ (*AKARI*/FIS). This allows a possible contribution of the host galaxy emission to the FIR bands, even when its contribution to the MIR flux is negligible as discussed in Section 3 (see also Lyu & Rieke 2017). Therefore, FIR photometry with higher sensitivity is crucial to quantify the host galaxy contribution for those sources.

4.2. IR Pure-AGN Candidates

Some sources show AGN-dominated SEDs even in the FIR bands. These sources are called IR pure-AGN (Mullaney et al. 2011; Rosario et al. 2012, 2018; Matsuoka & Woo 2015; Ichikawa et al. 2017), and they are ideal candidates for deriving intrinsic AGN IR templates. These IR pure-AGN have a spectral turnover at $20\text{--}40\ \mu\text{m}$ (Alonso-Herrero et al. 2012; Hönig et al. 2014; Fuller et al. 2016; Lopez-Rodriguez et al. 2018) and a declining flux density from $40\ \mu\text{m}$ to $160\ \mu\text{m}$, suggesting a very low contribution from the starburst in the host galaxy. In order to check the SED turnover quantitatively, we plot IR color-color plots of $f_{70\ \mu\text{m}}/f_{160\ \mu\text{m}}$ versus $f_{22\ \mu\text{m}}/f_{70\ \mu\text{m}}$ in Figure 4. Both flux ratios are known to be sensitive to the SED peak, and therefore to the dust temperature (Meléndez et al. 2014; García-González et al. 2016b). The orange shaded area in Figure 4 ($f_{70\ \mu\text{m}}/f_{160\ \mu\text{m}} > 1.0$ and $f_{22\ \mu\text{m}}/f_{70\ \mu\text{m}} > 1.0$)

indicates a decline in flux density as a function of wavelength from $22\ \mu\text{m}$ to $160\ \mu\text{m}$ since the sources fulfill $f_{22\ \mu\text{m}} > f_{70\ \mu\text{m}} > f_{160\ \mu\text{m}}$.

Figure 4 also shows the simulated IR color as a function of $f_{\text{AGN}}^{(\text{IR})}$ for each SB template. All IR colors follow a similar trend: $f_{22\ \mu\text{m}}/f_{70\ \mu\text{m}}$ increases up to $f_{22\ \mu\text{m}}/f_{70\ \mu\text{m}} \approx 1.0$ with $f_{\text{AGN}}^{(\text{IR})}$ up to 0.9, while $f_{70\ \mu\text{m}}/f_{160\ \mu\text{m}}$ shows a very shallow increase until $f_{\text{AGN}}^{(\text{IR})} \leq 0.8$. However, for $f_{\text{AGN}}^{(\text{IR})} > 0.9$, $f_{70\ \mu\text{m}}/f_{160\ \mu\text{m}}$ starts to drastically increase, reaching values up to ≈ 7.0 . Thus, sources located in the orange shaded area should have AGN-dominated IR SEDs with $f_{\text{AGN}}^{(\text{IR})} > 0.90$. In this study we define a source as IR pure-AGN when it fulfills the following criteria: (1) $f_{\text{AGN}}^{(\text{IR})} > 0.90$ and (2) a significant detection at both $60\text{--}70\ \mu\text{m}$ and $160\ \mu\text{m}$. A total of nine sources are selected with these criteria, and they are shown with the black crosses in Figure 4. Most IR pure-AGN are successfully located in the orange shaded area in the color-color plot. Figure 5 shows the SEDs of the nine selected IR pure-AGN. All sources show an SED turnover between $\approx 20\ \mu\text{m}$ and $\approx 70\ \mu\text{m}$, a declining flux density from $70\ \mu\text{m}$ to $160\ \mu\text{m}$, and no FIR bump due to star formation up to $90\ \mu\text{m}$, with the exception of Fairall 9 and II SZ 010. Some of the sources in our sample have already been reported as being dominated by emission from the torus in the IR from the study of their *Spitzer*/IRS spectra (e.g., MCG–05–23–16; Ichikawa et al. 2015), based on the spectral turnover at $20\text{--}40\ \mu\text{m}$ (Alonso-Herrero et al. 2012; Hönig et al. 2014; Fuller et al. 2016; Lopez-Rodriguez et al. 2018).

We also check the AGN properties of IR pure-AGN compared to the parent sample. The means and standard deviations of the logarithmic X-ray luminosity, black hole mass, and Eddington ratio of this subsample are $\langle \log L_{14-150} \rangle = 43.7 \pm 0.3$, $\langle \log M_{\text{BH}} \rangle = 7.8 \pm 0.5$, and $\langle \log \lambda_{\text{Edd}} \rangle = -1.2 \pm 0.3$, respectively. These values are consistent with those of the parent sample of $\langle \log L_{14-150} \rangle = 43.7 \pm 0.8$, $\langle \log M_{\text{BH}} \rangle = 8.0 \pm 0.8$, and $\langle \log \lambda_{\text{Edd}} \rangle = -1.5 \pm 0.8$. This result suggests that the dominant contribution of AGNs to the total IR band is not related to their higher AGN luminosities, lower BH masses, or higher Eddington ratio, while it implies that they have weaker star formation luminosities than other AGNs of similar luminosity. Actually, MCG–05–23–16 is one of the pure IR-AGN whose CO emission has not been detected (Rosario et al. 2018) in the *Swift*/BAT AGN subset of the LLAMA survey (Davies et al. 2015). This suggests that its host galaxy already

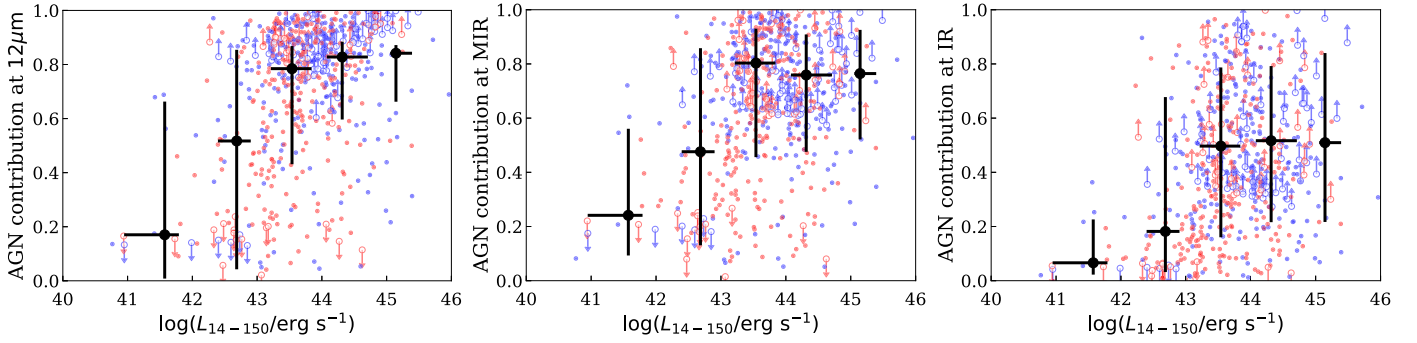


Figure 3. Fractional luminosity contribution of AGNs to the 12 μm (left), MIR (middle), and total IR (right) luminosities, as a function of 14–150 keV luminosity (L_{14-150}). The blue (unobscured AGNs) and red (obscured AGNs) circles represent individual sources. The circles with lower/upper limits represent the sources that require only the AGN or host galaxy template, as discussed in Section 3. The black crosses represent the median contribution of the AGN luminosity in each bin of L_{14-150} , with the error bars showing the inter-percentile range containing 68.2% of the sample.

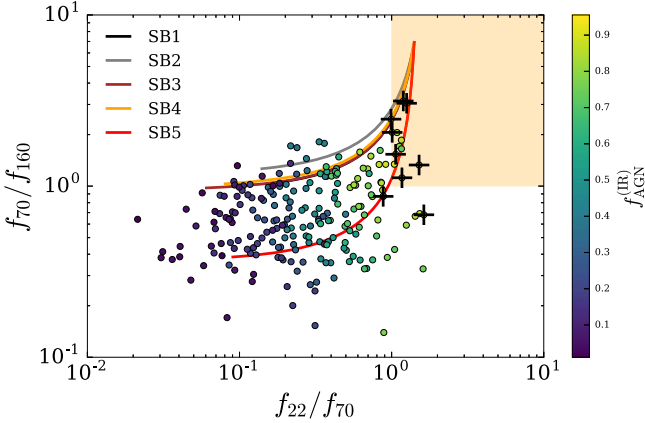


Figure 4. Observed ratio $f_{70\mu\text{m}}/f_{160\mu\text{m}}$ vs. $f_{22\mu\text{m}}/f_{70\mu\text{m}}$ for sample sources with secure detections in the 22 μm , 70 μm , and 160 μm bands. The color-color variations as a function of $f_{\text{IR}}^{(\text{AGN})}$ are also plotted for the five SB templates used in this study that originate from Mullaney et al. (2011). The black crosses are the IR pure-AGN sources discussed in Section 4.2. The color bar represents the AGN contribution to the total IR band ($f_{\text{IR}}^{(\text{AGN})}$). The orange area illustrates the region with $f_{22\mu\text{m}} > f_{70\mu\text{m}} > f_{160\mu\text{m}}$.

lacks the molecular gas to produce the star formation. The ongoing molecular gas observations conducted by the BASS survey (M. Koss et al. 2018, in preparation) will explore the origin of the deficit of star formation in these IR pure-AGN sources.

4.3. Correlation between the 12 μm AGN and 14–150 keV Luminosities

Figure 6 shows the relation between $L_{12\mu\text{m}}^{(\text{AGN})}$, $L_{\text{MIR}}^{(\text{AGN})}$, and L_{14-150} in the range $10^{40} \text{ erg s}^{-1} < L_{14-150} < 10^{47} \text{ erg s}^{-1}$. Blue and red crosses represent unobscured and obscured AGNs, respectively. The upper limits, shown as open circles, represent the host galaxy-dominated sources that have a possible AGN contribution in the 12 μm and MIR bands as discussed in Section 3. The slope of the relation between $L_{12\mu\text{m}}^{(\text{AGN})}$, $L_{\text{MIR}}^{(\text{AGN})}$, and L_{14-150} is estimated considering the two variables as independent parameters. Since our data contain both detections and upper limits, we apply the survival analysis method using the Python package²² ASURV (Feigelson & Nelson 1985; Isobe et al. 1986; Lavalley et al. 1992) to account for the upper limits on $L_{12\mu\text{m}}^{(\text{AGN})}$ and $L_{\text{MIR}}^{(\text{AGN})}$. We use the slope bisector fits, which

minimize the perpendicular distance from the slope line to data points. The fits, with the form of $\log(L_{12\mu\text{m}}^{(\text{AGN})}/10^{43} \text{ erg s}^{-1}) = (a \pm \Delta a) + (b \pm \Delta b) \log(L_{14-150}/10^{43} \text{ erg s}^{-1})$, where Δa and Δb are the standard deviations of a and b , respectively, result in

$$\log \frac{L_{12\mu\text{m}}^{(\text{AGN})}}{10^{43} \text{ erg s}^{-1}} = (-0.24 \pm 0.03) + (1.08 \pm 0.03) \times \log \frac{L_{14-150}}{10^{43} \text{ erg s}^{-1}}, \quad (2)$$

$$\log \frac{L_{\text{MIR}}^{(\text{AGN})}}{10^{43} \text{ erg s}^{-1}} = (-0.05 \pm 0.03) + (1.06 \pm 0.03) \times \log \frac{L_{14-150}}{10^{43} \text{ erg s}^{-1}}, \quad (3)$$

and they are also summarized in Table 2. We find that both luminosity–luminosity and flux–flux correlations are significant (see also Appendix B for the flux–flux correlations).

In Figure 6, some of the fits reported by recent works are also overplotted. Since most previous studies used the 2–10 keV luminosity, we apply a conversion factor of $L_{14-150}/L_{2-10} = 2.36$ under the assumption of the photon index $\Gamma = 1.8$, which is the median value of the *Swift*/BAT 70 month AGN sample (Ricci et al. 2017b), for overplotting in the same figure. Since the AGN template used in this study has a ratio of $L_{\text{MIR}}^{(\text{AGN})}/L_{12\mu\text{m}}^{(\text{AGN})} = 1.92$, we also apply it to the slopes from the previous studies for overplotting in the relation between $L_{\text{MIR}}^{(\text{AGN})}$ and L_{14-150} .

Compared to Ichikawa et al. (2017), where we found $b = 0.96 \pm 0.02$, the sample used here shows a smaller 12 μm contribution from AGN at the low-luminosity end. This is because the sources with lower L_{14-195} have a significant host galaxy contamination even in the MIR, as shown in Figure 3 and also in the right panel of Figure 11. Indeed, Ichikawa et al. (2017) also reported that the slope becomes slightly steeper with $b = 1.05 \pm 0.03$ when one considers sources with $L_{14-195} > 10^{43} \text{ erg s}^{-1}$, for which the host galaxy contamination in the MIR is negligible. This is also consistent with the value of $b = 1.08 \pm 0.03$ in this study.

We compare our results with what was found by Gandhi et al. (2009) and Asmus et al. (2015) using observations with high spatial resolution of X-ray-selected AGNs down to the low-luminosity end. The MIR emission in those studies is most likely dominated by the AGN torus, and they have a relatively

²² <http://python-asurv.sourceforge.net/>

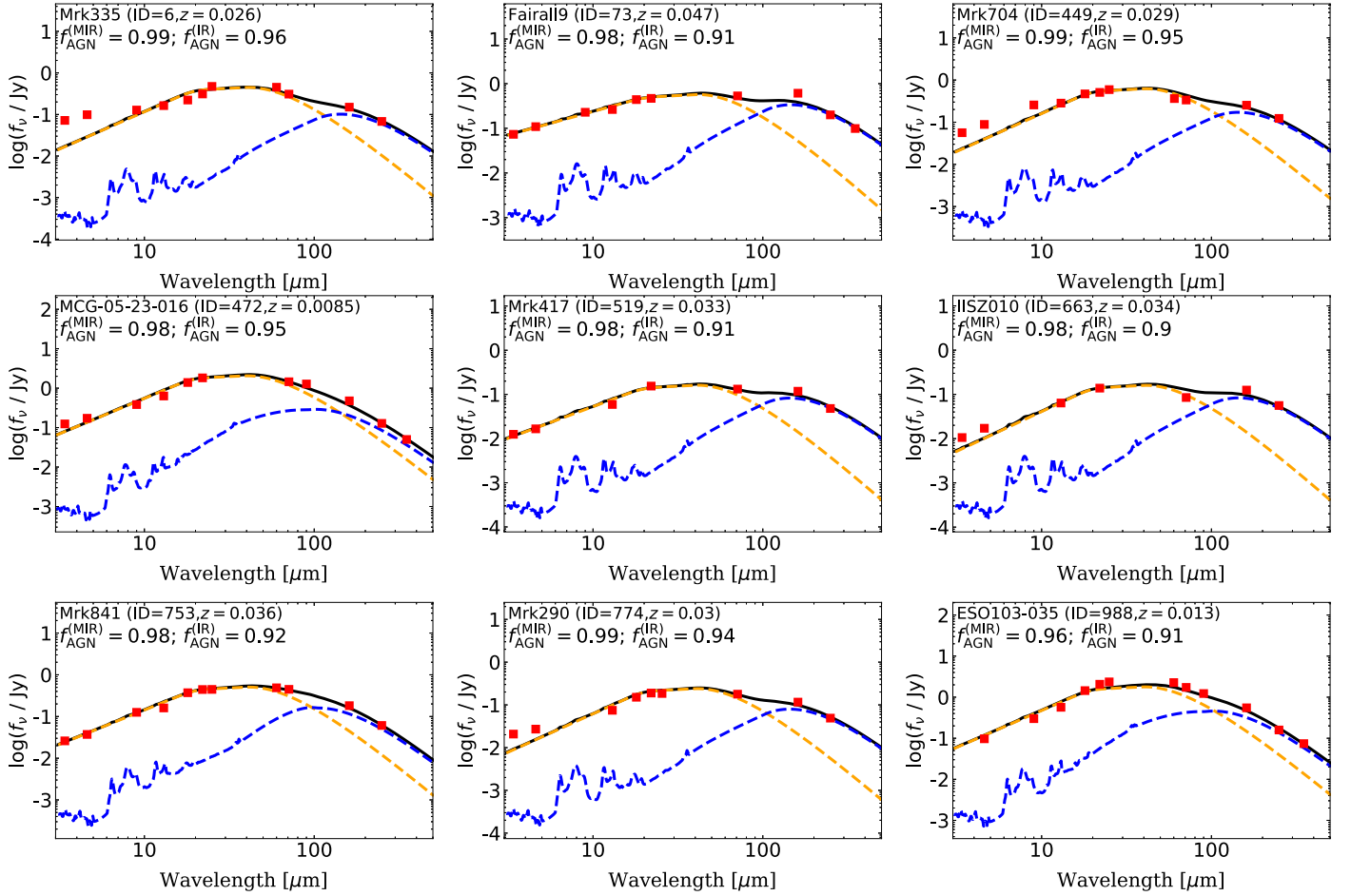


Figure 5. SEDs of the IR pure-AGN candidates defined by (1) $f_{\text{AGN}}^{(\text{IR})} > 0.90$ and (2) significant detection at both 60–70 μm and 160 μm . All plots are same as in Figure 2.

low level of host galaxy contamination thanks to their spatially resolved images. As shown in Figure 6, our study finds a similar slope to that reported in Gandhi et al. (2009) ($b = 1.11 \pm 0.07$), and it is also within the 3σ uncertainty of that of Asmus et al. (2015) ($b = 0.97 \pm 0.03$). This strongly supports the idea that our SED decomposition method nicely reproduces the flux at high spatial resolution, which is thought to be dominated by AGN torus emission.

4.4. Covering Factor of AGNs as a Function of Bolometric Luminosity

The ratio of the AGN IR luminosity and the AGN bolometric luminosity ($R = L_{\text{IR}}^{(\text{AGN})}/L_{\text{bol}}^{(\text{AGN})}$) has been interpreted as an indirect indicator of the dust covering factor ($C_{\text{T}}(\text{dust})$), since, for a given AGN luminosity, $L_{\text{IR}}^{(\text{AGN})}$ should be proportional to $C_{\text{T}}(\text{dust})$ ($L_{\text{IR}}^{(\text{AGN})} \propto C_{\text{T}}(\text{dust}) \times L_{\text{bol}}^{(\text{AGN})}$; Maiolino et al. 2007; Treister et al. 2008; Elitzur 2012). Since the flux of the accretion disk cannot be directly measured for all the sources of our sample, we used L_{14-150} to estimate the bolometric luminosity. We apply a constant bolometric correction of $L_{\text{bol}}^{(\text{AGN})}/L_{2-10} = 20$, which is equivalent to $L_{\text{bol}}^{(\text{AGN})}/L_{14-150} = 8.47$ under the assumption of $\Gamma = 1.8$, which is the median value of the *Swift*/BAT 70 month AGN sample (Ricci et al. 2017b). We note that our main results do not change significantly when adopting different bolometric

corrections, including luminosity-dependent ones (Marconi et al. 2004). We briefly discuss this in Appendix C.2.

To calculate R , we proceed in the same manner as Stalevski et al. (2016). We use the total IR AGN luminosity integrated over 1–1000 μm ($L_{\text{IR}}^{(\text{AGN}; 1-1000\mu\text{m})}$) instead of $L_{\text{IR}}^{(\text{AGN})}$, which integrates the SED over 5–1000 μm . This is because Stalevski et al. (2016) recommend using the AGN SEDs including NIR, which sometimes contributes to the total IR luminosity at a non-negligible level. Since we do not have an IR AGN template down to 1 μm , we extrapolate the AGN template using the same spectral index of α_1 used at wavelengths shorter than 19 μm . Therefore, R is calculated based on $R = L_{\text{IR}}^{(\text{AGN}; 1-1000\mu\text{m})}/L_{\text{bol}}^{(\text{AGN})}$ in the following study. Figure 7 shows the relation between R and the AGN bolometric luminosity. The black dashed line represents the fit obtained using ASURV to account for the sources with an upper limit:

$$\log R = (4.52 \pm 1.25) + (-0.12 \pm 0.03) \log \left(\frac{L_{\text{bol}}^{(\text{AGN})}}{\text{erg s}^{-1}} \right). \quad (4)$$

This shows that R is a very weak function of AGN bolometric luminosity. However, R does not always represent the actual $C_{\text{T}}(\text{dust})$, because the standard geometrically thin and optically thick disk emits radiation anisotropically (Netzer 1987; Lusso et al. 2013). Thus we also estimate $C_{\text{T}}(\text{dust})$ exploiting the recent results of Stalevski et al. (2016),

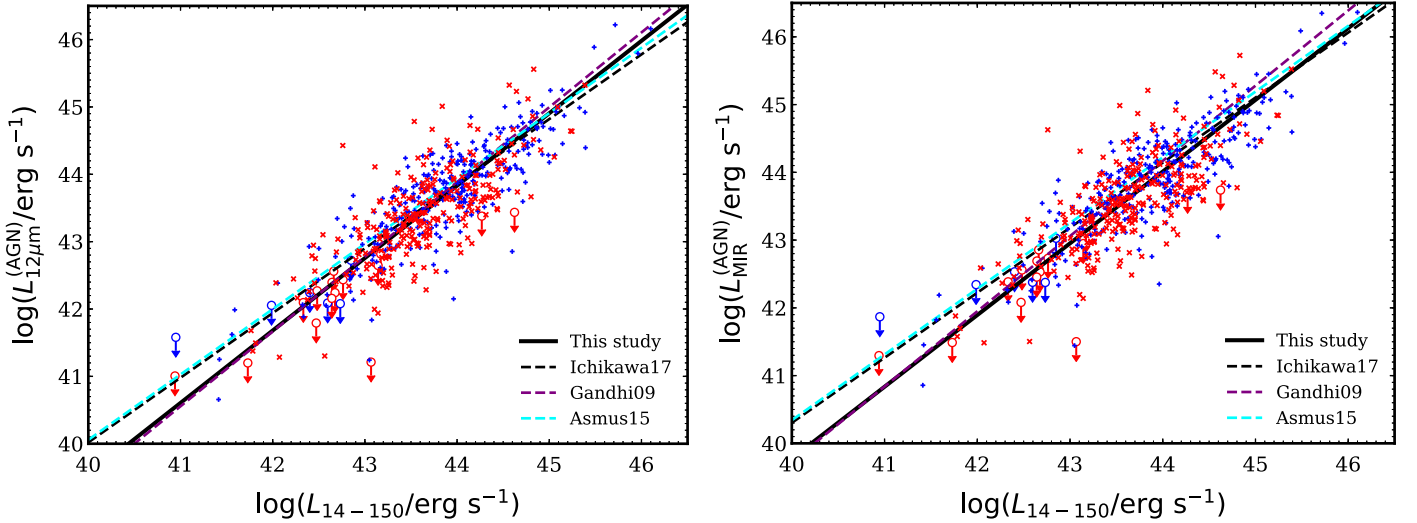


Figure 6. Scatter plot of the 14–150 keV (L_{14-150}) luminosity and the AGN 12 μ m ($L_{12\mu m}^{(AGN)}$; left panel) and MIR ($L_{MIR}^{(AGN)}$; right panel) luminosities. Blue and red crosses represent unobscured and obscured AGNs, respectively. The black solid line represents the slope obtained by this study using the infrared bands after the SED decomposition. The other lines represent the one obtained in our previous study before the SED decomposition (Ichikawa et al. 2017, black dashed line), and the studies with higher spatial resolution by Gandhi et al. (2009, purple) and Asmus et al. (2015, cyan).

who computed the correction function between the covering factor ($C_T(\text{dust})$) and R using a clumpy two-phase medium with a sharp boundary between the dusty and dust-free environments. They compute the $C_T(\text{dust})$ – R relation for a range of equatorial torus thickness ($\tau_{9.7} = 3$ –10). We consider here the function for $\tau_{9.7} = 3$:

$$C_T(\text{dust}) = \begin{cases} -0.178R^4 + 0.875R^3 - 1.487R^2 \\ \quad + 1.408R + 0.192 \text{ (type 1)} \\ 2.039R^3 - 3.976R^2 + 2.765R + 0.205 \text{ (type 2)}. \end{cases} \quad (5)$$

We use Equation (5) for type-1/type-2 AGN to unobscured/obscured AGNs in this study. According to Stalevski et al. (2016) the relations reported above are valid only for $R \leq R_{\text{max}}$, where $R_{\text{max}} = 1.3$ for unobscured AGNs and $R_{\text{max}} = 1.0$ for obscured AGNs, so we removed five sources with $R \geq R_{\text{max}}$ from the sample. Figure 8 shows $C_T(\text{dust})$ as a function of L_{bol} .

Besides the dust covering factor $C_T(\text{dust})$, we also calculate the fraction of obscured AGNs ($\log(N_H/\text{cm}^{-2}) \geq 22.0$), including the Compton-thick sources for each $L_{\text{bol}}^{(AGN)}$ bin as shown in Figure 8 (orange crosses). Since X-rays are absorbed by both gas and dust, the fraction of obscured AGNs is a proxy for the covering factor of the obscuring material, and is sensitive to both gas and dust [$C_T(\text{gas} + \text{dust})$].²³ We follow the same approach to obtain $C_T(\text{gas} + \text{dust})$ as done by Ricci et al. (2017a). The column density N_H for our sample is obtained through detailed X-ray spectral fitting using follow-up X-ray observations (Ricci et al. 2017b). In the X-ray fitting, both photoelectric absorption and Compton scattering are considered, and they are listed in Table 5 of Ricci et al. (2017b). $C_T(\text{gas} + \text{dust})$ is defined as $C_T(\text{gas} + \text{dust}) = f_{\text{Cthin}} + f_{\text{CT}}$, where f_{Cthin} is the fraction of

Compton-thin obscured AGNs ($22 \leq \log(N_H/\text{cm}^{-2}) < 24.0$) in each $L_{\text{bol}}^{(AGN)}$ bin, while the Compton-thick fraction is $f_{\text{CT}} = 0.32$ for $\log(L_{\text{bol}}^{(AGN)})/\text{erg s}^{-1} < 43.5$ and $f_{\text{CT}} = 0.21$ for $\log(L_{\text{bol}}^{(AGN)})/\text{erg s}^{-1} > 43.5$ obtained from the intrinsic N_H distribution (Ricci et al. 2015). The reason for using f_{CT} above is because even though *Swift*/BAT sources are unbiased for $N_H < 10^{24} \text{ cm}^{-2}$, they can still be affected by obscuration for $N_H > 10^{24} \text{ cm}^{-2}$.

4.4.1. $L_{\text{bol}}^{(AGN)}$ -dependent Trend of $C_T(\text{dust})$

Figure 8 shows that both $C_T(\text{dust})$ and $C_T(\text{gas} + \text{dust})$ seem to decrease as functions of AGN bolometric luminosity, and at the high-luminosity end the two finally converge. This luminosity-dependent trend of C_T has been observationally reported in multiple wavelengths from studies in the IR (e.g., Maiolino et al. 2007; Alonso-Herrero et al. 2011), optical (Simpson 2005), and X-rays (Ueda et al. 2003, 2011, 2014; Beckmann et al. 2009; Ricci et al. 2013).

However, recent studies have also reported contradictory results that the luminosity dependence of $C_T(\text{dust})$ is actually really weak, or that the trend even disappears after considering some possible biases. Netzer et al. (2016) argue that using the different bolometric corrections would make the reported luminosity dependence of $C_T(\text{dust})$ disappear. Stalevski et al. (2016) also found that the dependence on luminosity is always less pronounced after considering the anisotropy of the emission from the torus. A similar weak or insignificant dependence on luminosity is reported by Mateos et al. (2016), and a more detailed review is given by Netzer (2015).

In order to understand this trend in more detail, we conduct a simulation to assess the luminosity dependence of $C_T(\text{dust})$. We first generate the two random populations of L_{14-150} for unobscured and obscured AGNs in a total of 10^4 samples with the same number ratio as our parent sample (unobscured/obscured = 300/287; see Section 2). Each sample is generated based on our parent sample, using a Gaussian distribution with median $\log(L_{14-150}/\text{erg s}^{-1})$ of (43.9, 43.6) and standard deviation of (0.85 dex, 0.67 dex) for unobscured and obscured AGNs, respectively. Then the distribution of $L_{\text{IR}}^{(AGN; 1-1000\mu\text{m})}$ is

²³ Although the dusty region also contains the gas, in this study we use $C_T(\text{dust})$ as the covering area of dust which is heated by AGN, and re-emits the IR. We then use $C_T(\text{gas} + \text{dust})$ as the covering area of gas that is responsible for the X-ray absorption. This region includes (1) the dusty region defined by $C_T(\text{dust})$ since that region also includes the gas, and (2) the dust-free region that is inside the sublimation radius but contains the neutral gas.

Table 2
Equations of the Correlation in This Study

(1) Y	(2) X	(3) a	(4) b	(5) Reference
$\log \left(\frac{L_{12\mu\text{m}}^{(\text{AGN})}}{10^{43} \text{ erg s}^{-1}} \right)$	$\log \left(\frac{L_{14-150}}{10^{43} \text{ erg s}^{-1}} \right)$	-0.24 ± 0.03	1.08 ± 0.03	Section 4.3
$\log \left(\frac{L_{\text{MIR}}^{(\text{AGN})}}{10^{43} \text{ erg s}^{-1}} \right)$	$\log \left(\frac{L_{14-150}}{10^{43} \text{ erg s}^{-1}} \right)$	-0.05 ± 0.03	1.06 ± 0.03	Section 4.3
$\log R$	$\log \left(\frac{L_{\text{bol}}^{(\text{AGN})}}{\text{erg s}^{-1}} \right)$	4.52 ± 1.25	-0.12 ± 0.03	Section 4.4

Note. Correlation properties between two physical values. Columns: (1) Y variable; (2) X variable; (3) regression intercept (a) and its 1σ uncertainty; (4) slope (b) and its 1σ uncertainty; the equation is represented as $Y = a + bX$; (5) reference for the details of each equation.

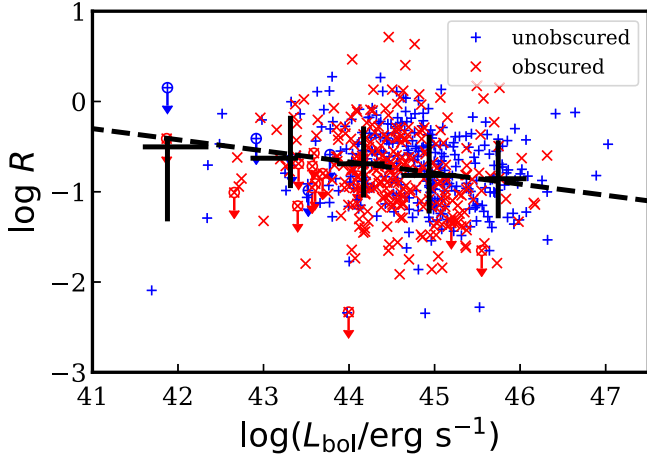


Figure 7. $R = L_{\text{IR}}^{(\text{AGN}; 1-1000\mu\text{m})}/L_{\text{bol}}^{(\text{AGN})}$ as a function of the bolometric luminosity. The black crosses represent the median value of R in each bin of bolometric luminosity, with the error bars showing the inter-percentage range containing 68.2% of the sample.

calculated under the assumption that two populations follow the luminosity correlation of $L_{\text{IR}}^{(\text{AGN}; 1-1000\mu\text{m})}-L_{14-150}$ with a scatter of $\sigma = 0.4$ dex, and finally the distribution of $C_{\text{T}}(\text{dust})$ is computed in the same manner. The result is shown in Figure 9: the computed $C_{\text{T}}(\text{dust})$ distribution (gray cross bins) roughly reproduces the luminosity dependence of the black solid bins. Next, we assume that all AGNs should follow the luminosity correlation of $L_{\text{IR}}^{(\text{AGN}; 1-1000\mu\text{m})}-L_{14-150}$ and the intrinsic population should have the narrower scatter, down to $\sigma = 0.1$ dex. The result is plotted with pink bins in Figure 9, showing that the luminosity dependence has disappeared and the binned $C_{\text{T}}(\text{dust})$ has an almost constant value of $C_{\text{T}}(\text{dust}) \simeq 0.4$ over the entire $L_{\text{bol}}^{(\text{AGN})}$ range. Therefore, we conclude that this apparent dependence on luminosity can be produced purely by the scatter of the distribution, and our results confirm the recent arguments that the luminosity dependence of $C_{\text{T}}(\text{dust})$ is actually really weak, or that the trend even disappears.

4.4.2. Relation between $C_{\text{T}}(\text{dust})$ and $C_{\text{T}}(\text{gas} + \text{dust})$

The other interesting result from Figure 8 is that $C_{\text{T}}(\text{gas} + \text{dust})$ is always same as or larger than the binned $C_{\text{T}}(\text{dust})$ over the entire AGN luminosity range. This relation

still holds if $C_{\text{T}}(\text{dust}) \simeq 0.4 \leq C_{\text{T}}(\text{gas} + \text{dust})$ in our simulation as shown in Figure 9. This result suggests the presence of dust-free gas, possibly located in the broad-line region (BLR), and is responsible for part of the X-ray absorption. Observationally, using long-term X-ray data, Markowitz et al. (2014) found evidence of occultation events in the X-rays, and the locations of those gas clumps are in the dust-free region or at the inner edge of the dusty torus (e.g., Risaliti et al. 2007, 2011; Maiolino et al. 2010; Ricci et al. 2016). In addition, Minezaki & Matsushita (2015) and Gandhi et al. (2015) have suggested that the location of narrow Fe $K\alpha$ line-emitting material could be between the BLR and the dusty torus. Those observations imply the presence of gas at radii inside the sublimation radius. Several studies have also proposed that the AGN gas disk inside the dust sublimation radius could significantly contribute to the observed column density in Compton-thick AGNs, since such disks are often found to have large inclination angles (e.g., Davies et al. 2015; Masini et al. 2016; Ramos Almeida & Ricci 2017). We also check whether the similar trend of $C_{\text{T}}(\text{dust}) \leq C_{\text{T}}(\text{gas} + \text{dust})$ can be seen using only the MIR fluxes before the SED decomposition. This is discussed in Appendix C.1.

Figure 8 also shows that both $C_{\text{T}}(\text{dust})$ and $C_{\text{T}}(\text{gas} + \text{dust})$ seem to suggest a peak at $\log L_{\text{bol}} \simeq 43$, and they both seem to decrease at lower luminosities. However, since the number of samples is limited in this bin range, we cannot confirm the statistical significance of this trend at the current stage (see also the discussion in Appendix C.2).

4.4.3. Comparison of $C_{\text{T}}(\text{dust})$ between Unobscured and Obscured AGNs

We compare $C_{\text{T}}(\text{dust})$ between the AGN subgroups. The left panel of Figure 10 shows $C_{\text{T}}(\text{dust})$ of unobscured (blue) and obscured (red) AGNs as a function of $L_{\text{bol}}^{(\text{AGN})}$. Although the scatter is large, the binned $C_{\text{T}}(\text{dust})$ of obscured AGNs is always systematically higher than that of unobscured AGNs.

The right panel of Figure 10 shows the distribution of $C_{\text{T}}(\text{dust})$ for unobscured (blue) and obscured (red) AGNs. The $C_{\text{T}}(\text{dust})$ distribution for unobscured AGNs is clustered at smaller values of $\langle C_{\text{T}}(\text{dust}) \rangle = 0.41$, while obscured AGNs are distributed over a wider $C_{\text{T}}(\text{dust})$ range, reaching $C_{\text{T}}(\text{dust}) \simeq 1.0$. We apply the Kolmogorov–Smirnov (KS) test to these two samples: the p -value of the null hypothesis is 5.7×10^{-8} and the KS statistic is 0.24, suggesting that the two distributions are

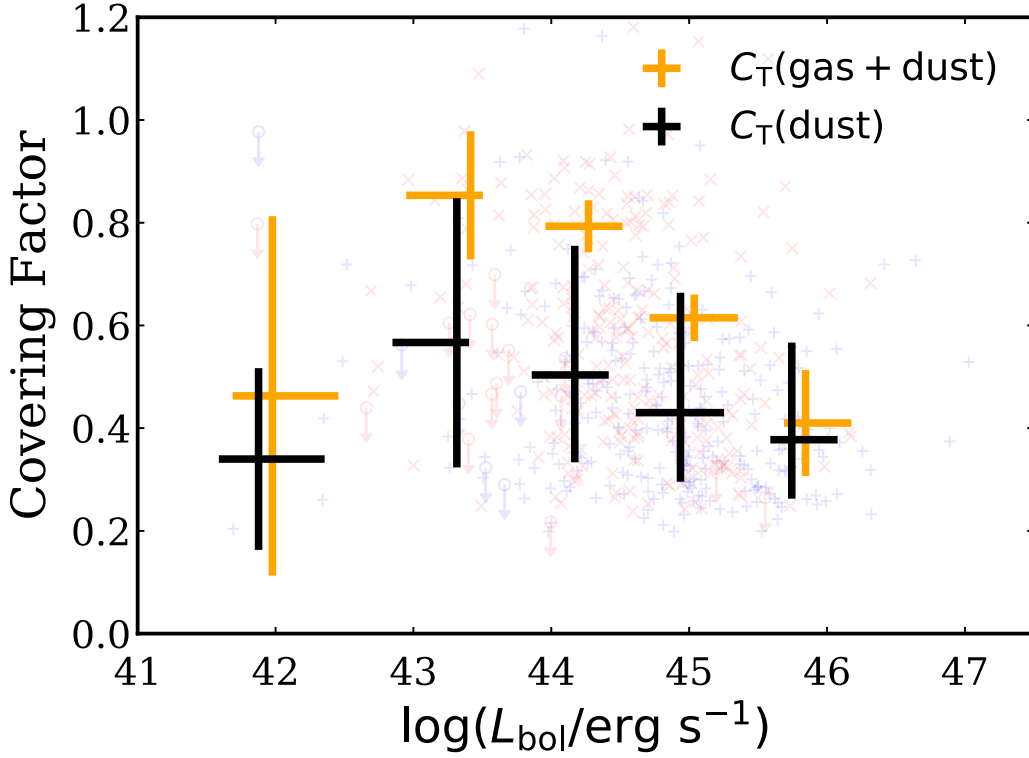


Figure 8. The covering factor (C_T) as a function of the bolometric luminosity. The dust covering factors $C_T(\text{dust})$ are obtained from R using the corrections reported in Stalevski et al. (2016). The covering factors of gas and dust $C_T(\text{gas}+\text{dust})$ are obtained from the X-ray observations and the spectral fitting based on the obscured AGN fraction including Compton-thick AGNs (Ricci et al. 2015, 2017b). The Compton-thick fraction is $f_{CT} = 0.32$ for $\log(L_{bol}^{(AGN)}/\text{erg s}^{-1}) < 43.5$ and $f_{CT} = 0.21$ for $\log(L_{bol}^{(AGN)}/\text{erg s}^{-1}) > 43.5$. The orange crosses are shifted to the right by 0.1 dex for clarity.

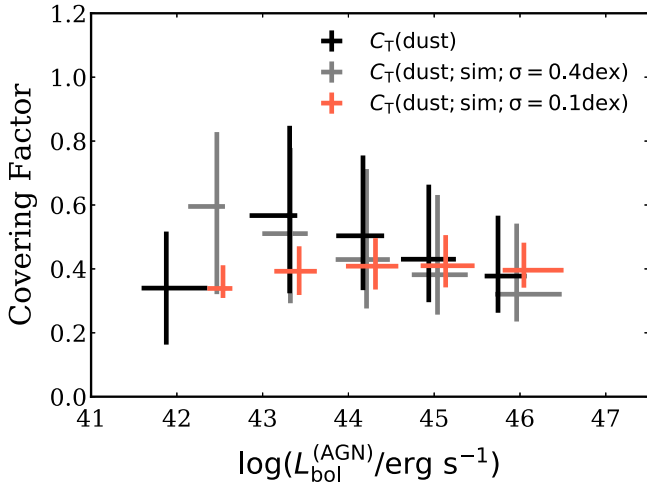


Figure 9. The dust covering factor ($C_T(\text{dust})$) as a function of the bolometric luminosity. The simulated dust covering factor $C_T(\text{dust}; \text{sim})$ is obtained from the simulation using a random population following the $L_{IR}^{(AGN)}-L_{14-150}$ relation with a scatter of $\sigma = 0.4$ dex (gray crosses) and $\sigma = 0.1$ dex (pink crosses). The gray/pink crosses are shifted to the right by 0.1/0.2 dex for clarity.

significantly different, assuming that the significance level is $\alpha = 0.05$.

One possible origin of the difference is that the smaller $C_T(\text{dust})$ for unobscured AGNs could be due to larger $L_{bol}^{(AGN)}$. However, as discussed in Section 4.4.1, the luminosity dependence of $C_T(\text{dust})$ is unlikely, and the KS test shows that the distribution of $C_T(\text{dust})$ for unobscured and obscured AGNs is

statistically significant even in each $L_{bol}^{(AGN)}$ bin for $42.5 < \log(L_{bol}^{(AGN)}/\text{erg s}^{-1}) < 47$, with p -values of $p < 10^{-5}$ for $42.5 < \log(L_{bol}^{(AGN)}/\text{erg s}^{-1}) < 45.5$ and $p = 0.02$ for $45.5 < \log(L_{bol}^{(AGN)}/\text{erg s}^{-1}) < 47$.

Another possible interpretation of the difference is as a consequence of the selection of unobscured and obscured AGNs. Several authors argue that AGN classification depends on the distribution of $C_T(\text{dust})$; unobscured AGNs would be preferentially observed from AGNs with lower $C_T(\text{dust})$, and obscured AGNs from AGNs with higher $C_T(\text{dust})$ (e.g., Ramos Almeida et al. 2011; Elitzur 2012; Ichikawa et al. 2015; Lanz et al. 2018).

5. Conclusions

We have constructed the IR (3–500 μm) SED for 587 nearby AGNs detected in the 70 month *Swift*/BAT all-sky survey. Using this almost complete (587 out of 606; 94%) sample, we have decomposed the IR (3–500 μm) SEDs into SB and AGN components. The decomposition enabled us to estimate the AGN contribution to the 12 μm ($L_{12\mu\text{m}}^{(AGN)}$), MIR ($L_{MIR}^{(AGN)}$), and total IR ($L_{IR}^{(AGN)}$) luminosities, as well as the contribution of AGN luminosity to the 12 μm ($f_{AGN}^{(12\mu\text{m})}$), MIR ($f_{AGN}^{(MIR)}$), and total IR ($f_{AGN}^{(IR)}$) emission. Our results are summarized as follows.

1. The luminosity contribution of the AGN to the 12 μm , MIR, and total IR band flux increases with the 14–150 keV luminosity. The AGN contributions to the 12 μm , MIR, and total IR are almost 80%, 80%, and 50% at the high-luminosity end, respectively.

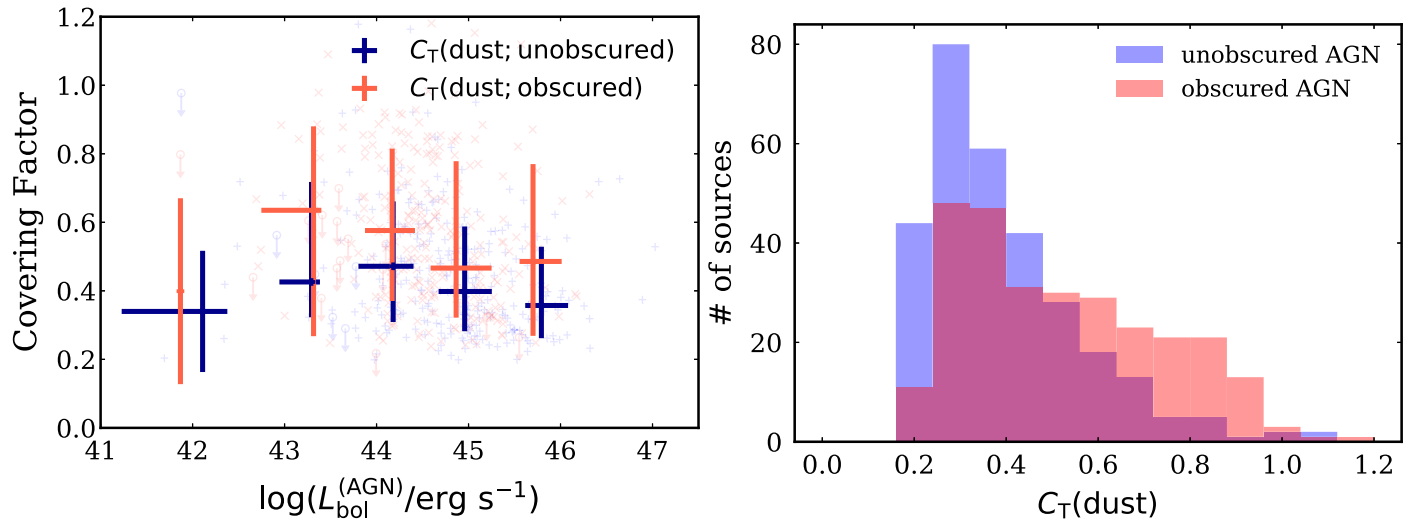


Figure 10. Left: the dust covering factor $C_T(\text{dust})$ of unobscured (blue) and obscured (red) AGNs as a function of the bolometric luminosity. Right: the distribution of $C_T(\text{dust})$ of unobscured and obscured AGNs.

2. We find nine pure IR-AGN whose IR emission is dominated by the AGN torus at least up to $90\ \mu\text{m}$. These pure IR-AGN could be good candidates to create templates of the IR AGN SED, with an expanded range up to $90\ \mu\text{m}$. Those sources could be easily selected using the color selection of $f_{70\mu\text{m}}/f_{160\mu\text{m}} > 1.0$ and $f_{22\mu\text{m}}/f_{70\mu\text{m}} > 1.0$.
3. We find a good luminosity correlation between the MIR and ultrahard X-ray bands over five orders of magnitude ($41 < \log(L_{14-150}/\text{erg s}^{-1}) < 46$). Our slope is almost consistent with that obtained by studies carried out using observations with high spatial resolution of nearby Seyfert galaxies, supporting our SED decomposition method, which would nicely estimate the intrinsic MIR emission without the contamination of star formation from the host galaxies.
4. We find that the average of the covering factor of gas and dust inferred from X-ray observations always exceeds the average of the covering factor of the dust torus, suggesting that the dust-free gas contributes to the absorption in X-rays. This gas could be located inside the dust sublimation radius, in agreement with previous observations based on X-ray occultation and spectral fitting studies of nearby AGNs.
5. The luminosity-dependent trend of $C_T(\text{dust})$ might originate from the large scatter of the luminosity correlations between $L_{\text{IR}}^{(\text{AGN}; 1-1000\mu\text{m})}$ and L_{14-150} , and the trend would disappear once the scatter is removed.
6. Obscured AGNs tend to have larger $C_T(\text{dust})$ than unobscured AGNs. This difference originates from the AGN classification, which depends on the distribution of the obscuring material.

We thank the anonymous referee for a careful reading of the manuscript and helpful suggestions that greatly strengthened the paper. We thank James Mullaney and Agnese Del Moro for providing the SB SED templates in this study, and Satoshi Takeshige for the technical discussion of IDL routine. We also thank Masatoshi Imanishi, Ryo Tazaki, and Daniel Asmus for

fruitful discussions. K.I. thanks the Department of Astronomy at Kyoto university, where a part of the research was conducted. This study benefited from financial support from the Grant-in-Aid for JSPS fellow for young researchers (P.D., K.I.), JSPS KAKENHI (18K13584; K.I.), and JST grant “Building of Consortia for the Development of Human Resources in Science and Technology” (K.I.). C.R. acknowledges the CONICYT+PAI Convocatoria Nacional subvencion a instalacion en la academia convocatoria año 2017 PAI77170080. F.E.B. acknowledges support from CONICYT-Chile (Basal-CATA PFB-06/2007, FONDECYT Regular 1141218), the Ministry of Economy, Development, and Tourism’s Millennium Science Initiative through grant IC120009, awarded to The Millennium Institute of Astrophysics, MAS. K.O. is an International Research Fellow of the Japan Society for the Promotion of Science (JSPS) (ID: P17321). D.J.R. acknowledges the support of UK Science and Technology Facilities Council through grant code ST/P000541/1.

Appendix A Comparison with Studies from the Literature

A.1. Comparison with the High-spatial-resolution Flux Obtained with Ground-based 8 m Class Telescopes

Here we compare the results in this study with the high-spatial-resolution observations by Asmus et al. (2014, 2015). Out of 122 high-spatial-resolution sources, we found 112 sources also used in this study. The remaining 10 sources were not found because they are located at low Galactic latitudes $|b| < 10^\circ$, which we initially removed from the parent sample as discussed in Ichikawa et al. (2017).

The top left panel of Figure 11 shows the $12\ \mu\text{m}$ luminosity correlation between the high-spatial-resolution MIR observations ($L_{12\mu\text{m}}^{(\text{Asmus})}$; Asmus et al. 2014, 2015) and this study after the SED decomposition ($L_{12\mu\text{m}}^{(\text{AGN})}$). The figure clearly shows that our decomposition method successfully follows the one-to-one relation with the high-spatial-resolution observations down to

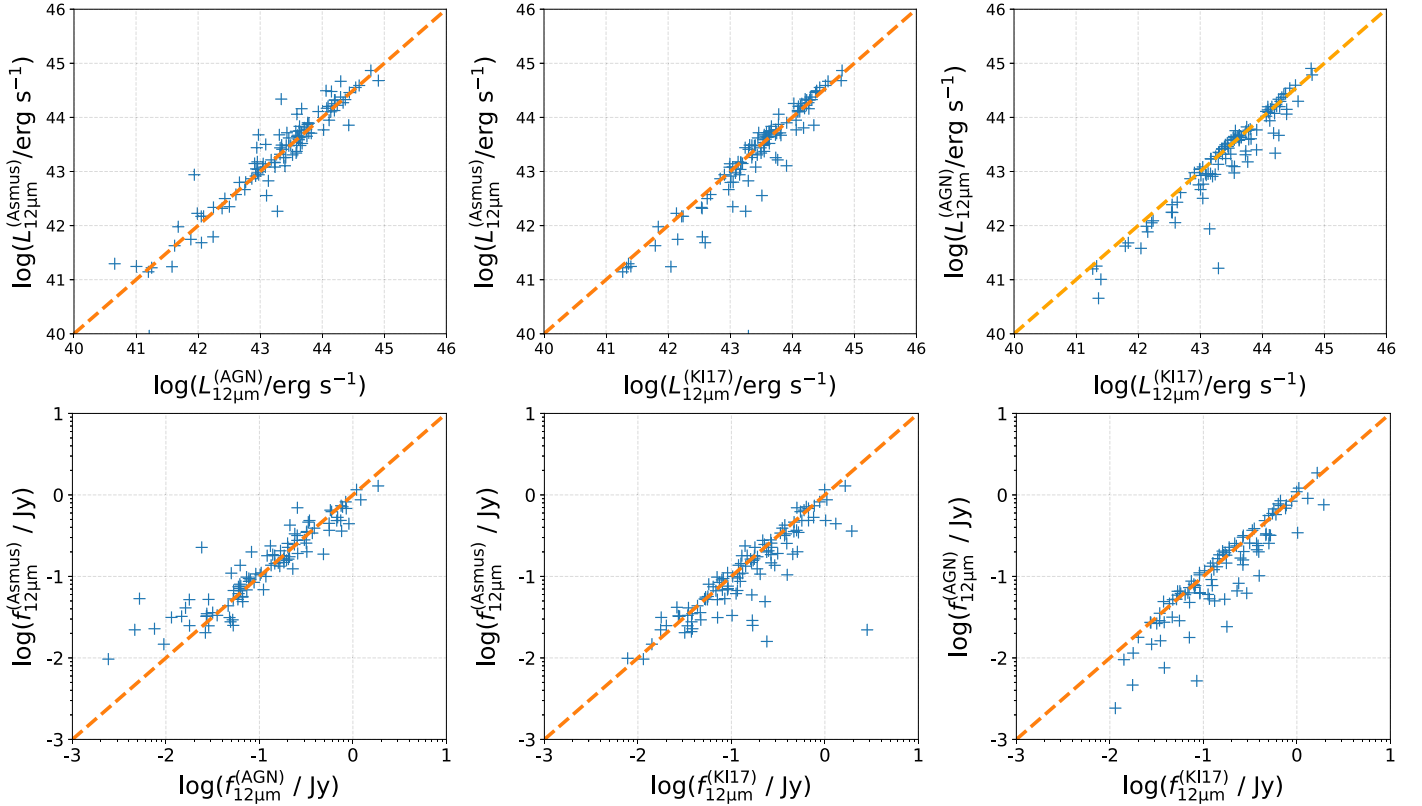


Figure 11. Top: scatter plot of the 12 μm luminosities obtained from high-spatial-resolution MIR observations ($L_{12\mu\text{m}}^{\text{(Asmus)}}$; Asmus et al. 2014, 2015), this study after the SED decomposition ($L_{12\mu\text{m}}^{\text{(AGN)}}$), and before the SED decomposition ($L_{12\mu\text{m}}^{\text{(KI17)}}$; Ichikawa et al. 2017). Blue crosses represent individual sources, and the orange dashed line represents the 1:1 relation. Panel show the luminosity relations between $L_{12\mu\text{m}}^{\text{(Asmus)}}$ and $L_{12\mu\text{m}}^{\text{(AGN)}}$ (left), $L_{12\mu\text{m}}^{\text{(Asmus)}}$ and $L_{12\mu\text{m}}^{\text{(KI17)}}$ (middle), $L_{12\mu\text{m}}^{\text{(AGN)}}$ and $L_{12\mu\text{m}}^{\text{(KI17)}}$ (right). Bottom: same plots as top but for 12 μm flux densities.

$\log(L_{12\mu\text{m}}^{\text{(AGN)}}/\text{erg s}^{-1}) \simeq 41.0$. The average of two parameters is $\langle \log L_{12\mu\text{m}}^{\text{(Asmus)}}/L_{12\mu\text{m}}^{\text{(AGN)}} \rangle = 0.05$. The standard deviation is $\sigma = 0.36$.

The top middle and top right panels of Figure 11 show the luminosity relation between $L_{12\mu\text{m}}^{\text{(Asmus)}}$, $L_{12\mu\text{m}}^{\text{(AGN)}}$, and the low-resolution 12 μm luminosity before the SED decomposition ($L_{12\mu\text{m}}^{\text{(KI17)}}$), which is taken from Ichikawa et al. (2017). Both panels show that the points are distributed equally to or below the one-to-one relations and suggest contamination of the host galaxy component in $L_{12\mu\text{m}}^{\text{(KI17)}}$. The mean and standard deviation are $\langle \log L_{12\mu\text{m}}^{\text{(Asmus)}}/L_{12\mu\text{m}}^{\text{(KI17)}} \rangle = -0.10 \pm 0.43$. This shows that the correlation between $L_{12\mu\text{m}}^{\text{(Asmus)}}$ and $L_{12\mu\text{m}}^{\text{(AGN)}}$ is tighter than that between $L_{12\mu\text{m}}^{\text{(Asmus)}}$ and $L_{12\mu\text{m}}^{\text{(KI17)}}$, indicating that our decomposition method nicely reduces the contamination in the 12 μm band from the host galaxies.

The bottom panels of Figure 11 show the same relations as those in the top panels, but for 12 μm flux densities. All three panels also show a similar trend to the luminosity relations. One notable difference is that the flux density of the high-spatial-resolution observation ($f_{12\mu\text{m}}^{\text{(Asmus)}}$) shows a decline in the number of sources at around $f_{12\mu\text{m}}^{\text{(Asmus)}} \simeq 10^{-2}$ Jy. This is almost consistent with the lower bound of the flux density observable with ground-based 8 m class telescopes with significant signal-to-noise ratio (Asmus et al. 2014). Our study can explore flux

densities down to 10^{-3} Jy, which is equivalent to the detection limit of the *WISE* W3 (12 μm) band. This is one of the advantages of the SED decomposition method using low-resolution, but sensitive space IR satellites compared to ground-based studies.

A.2. Comparison with Different Models from the Literature

In this appendix we briefly compare the IR AGN luminosity obtained in this study and the ones obtained in Shimizu et al. (2017). They applied a different IR SED model to the IR data set, which is similar to ours but obtained from the *Herschel* observations in the *Swift*/BAT 58 month AGN catalog to study mainly the global star-forming properties in the host galaxies. Instead of using the AGN/host galaxy templates, they provided functions of the hot dust and the host galaxy respectively by following Casey (2012), and their functions are given by

$$f(\nu) = N_{\text{pl}} \left(\frac{\nu}{\nu_c} \right) e^{-(\nu_c/\nu)^2} + S_{\text{MBB}}(\nu, M_{\text{dust}}, T_{\text{dust}}), \quad (6)$$

where the first term stands for the AGN component with the normalization N_{pl} and cut-off frequency ν_c , and the second term represents the host galaxy component of a single modified blackbody with a parameter of dust mass M_{dust} and a dust temperature T_{dust} . The fitting method used in their study is also different from ours. They use a Bayesian framework with a

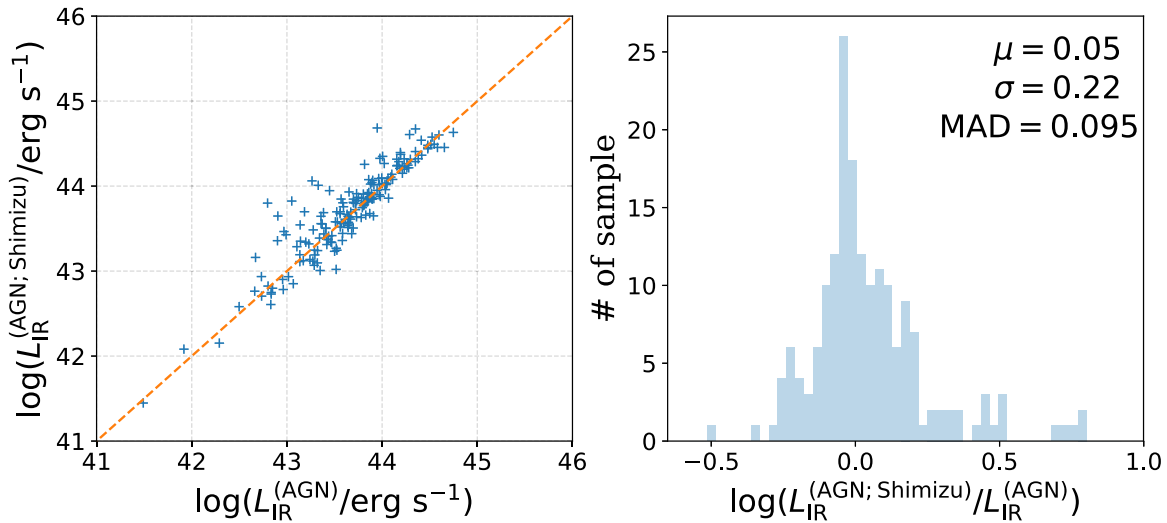


Figure 12. Left: scatter plot of total IR AGN luminosities obtained from Shimizu et al. (2017) ($L_{\text{IR}}^{(\text{AGN}; \text{Shimizu})}$) and those obtained from this study ($L_{\text{IR}}^{(\text{AGN})}$). Blue crosses represent individual sources, and the orange dashed line represents the 1:1 relation. Right: histogram of $r = \log(L_{\text{IR}}^{(\text{AGN}; \text{Shimizu})} / L_{\text{IR}}^{(\text{AGN})})$. The mean μ , standard deviation σ , and median absolute deviation (MAD) of r are also shown.

Markov chain Monte Carlo procedure to obtain the posterior probability distribution function, and then use the median to obtain the best fitted parameters. Out of 307 sources in their sample, 204 sources have at least one *Herschel* detection and a reliable fitting quality (`lir_agn_flag` = 0). After cross-matching with our sample, we found 180 sources in common. Again, the 24 sources removed are located at low Galactic latitude $|b| < 10^\circ$.

Since Shimizu et al. (2017) do not provide any $12\ \mu\text{m}$ AGN flux or luminosity, we compare the total IR AGN luminosity obtained from their AGN component. The left panel of Figure 12 shows the correlation between the IR AGN luminosities obtained from Shimizu et al. (2017) ($L_{\text{IR}}^{(\text{AGN}; \text{Shimizu})}$) and the ones from this study ($L_{\text{IR}}^{(\text{AGN})}$). The Spearman's rank coefficient is 0.91, and probability of the null hypothesis is $P = 4.9 \times 10^{-69}$, suggesting that the correlation is significant. The average of the distribution of $r = \log(L_{\text{IR}}^{(\text{AGN}; \text{Shimizu})} / L_{\text{IR}}^{(\text{AGN})})$ is also shown in the right panel of Figure 12. We do not find any systematic offset between the two methods ($\mu = 0.05$) with a standard deviation of $\sigma = 0.22$ dex. Since there are several outliers with $\log(L_{\text{IR}}^{(\text{AGN}; \text{Shimizu})} / L_{\text{IR}}^{(\text{AGN})}) > 0.3$, we also compute the median absolute deviation (MAD) and the value is $\text{MAD} = 0.095$ dex, which is smaller than the standard deviation by a factor of two. As already mentioned in Shimizu et al. (2017), their model

allows the power-law component to extend to longer wavelengths, which would return slightly larger AGN luminosities with $\log(L_{\text{IR}}^{(\text{AGN}; \text{Shimizu})} / L_{\text{IR}}^{(\text{AGN})}) > 0.3$ for some cases. Those sources are actually seen in Figure 12 but they are only a small percentage of the sample. Thus, we conclude that, although the fitting methods and the template are different, each model returns the consensus results for the estimation of the IR AGN luminosities.

Appendix B

Flux Correlation between $12\ \mu\text{m}$, MIR, and 14–150 keV Bands

Figure 13 shows the flux correlation between the AGN $12\ \mu\text{m}$, MIR, and 14–150 keV bands, revealing a clear correlation between the bands even in the flux–flux plane. The Spearman's rank coefficient is 0.43 and the probability of the null hypothesis is $P = 10^{-28}$ for both flux–flux correlations, suggesting that the correlation is significant. The slopes are $b = 1.48$ for the AGN $12\ \mu\text{m}$ band and $b = 1.49$ for the AGN MIR band, respectively. As we discussed in Ichikawa et al. (2017), there is a clear decline in the number of sources at $f_{14-150} < 10^{-11}\ \text{erg s}^{-1}\ \text{cm}^{-2}$, while MIR flux can go down to $3 \times 10^{-13}\ \text{erg s}^{-1}\ \text{cm}^{-2}$, which is the typical detection limit of the MIR band. This trend suggests that the sample is limited by the detection limit of the X-ray flux.

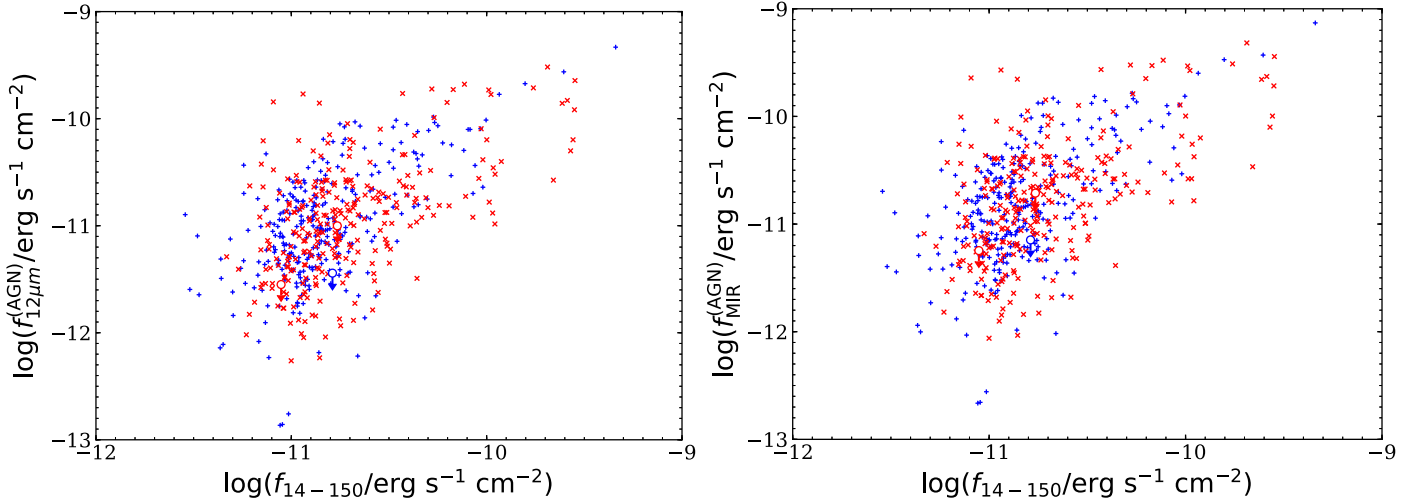


Figure 13. Correlation between the fluxes in the 12 μ m, MIR, and 14–150 keV bands. Blue and red crosses represent unobscured and obscured AGNs, respectively.

Appendix C

Comparison of Relation between C_T and $L_{bol}^{(AGN)}$ using Different Values

C.1. $C_T(\text{dust})$ Estimated from the Observed 12 μ m Luminosity

It is important to check whether the same result in Figure 8 is obtained using the MIR fluxes without host galaxy subtraction. To achieve this, we estimate the total IR AGN luminosity by assuming that the observed 12 μ m luminosity originates from the AGN emission. Then we use the conversion factor of $L_{IR}^{(AGN; 1-1000\mu m)}/L_{12\mu m}^{(AGN)} = 2.77$ estimated from the AGN template in this study. The calculation of R and then $C_T(\text{dust})$ is performed in the same manner as we discussed in Section 4.4. The left panel of Figure 14 shows the relation between C_T and $L_{bol}^{(AGN)}$ using $C_T(\text{dust})$ estimated above. It clearly shows that while the result $C_T(\text{dust}) < C_T(\text{gas} + \text{dust})$ holds for $43.5 < \log L_{bol}^{(AGN)} < 45.5$, $C_T(\text{dust})$ becomes almost equal to $C_T(\text{gas} + \text{dust})$ in the luminosity bin $42.5 < \log L_{bol}^{(AGN)} < 43.5$, which is not seen in Figure 8. We also apply the KS test between $C_T(\text{dust})$ and $C_T(\text{gas} + \text{dust})$ for each $L_{bol}^{(AGN)}$ luminosity bin. In order to apply this test, we make a Gaussian distribution of $C_T(\text{gas} + \text{dust})$ in which the central value is the average of $C_T(\text{gas} + \text{dust})$ and 1σ is its standard deviation, and the number of sources is the same as for $C_T(\text{dust})$ in the same $L_{bol}^{(AGN)}$ bin. As a result, we find a significant difference for the luminosity bins with $43.5 < \log L_{bol}^{(AGN)} < 45.5$ with p -values of $p < 10^{-30}$, while the clear significance is not obtained for the luminosity bins $\log L_{bol}^{(AGN)} < 43.5$ ($p > 0.5$) and $45.5 < \log L_{bol}^{(AGN)}$ ($p = 0.26$). This difference originates from the flux subtraction after the SED decomposition, especially at the lower AGN luminosity end, suggesting its importance and its effect on estimating the dust covering factor.

C.2. Dependence of the Bolometric Corrections

Here we summarize whether different bolometric corrections can affect the relation shown in Figure 8. In this study, following the method used in Ricci et al. (2017a), we use a constant bolometric correction of $L_{bol}^{(AGN)}/L_{14-150} = 8.47$, which is based on $L_{bol}^{(AGN)}/L_{2-10} = 20$ under the assumption of $\Gamma = 1.8$, the median value of the *Swift*/BAT 70 month AGN

sample (Ricci et al. 2017b). On the other hand, Marconi et al. (2004) account for variations in AGN SEDs to obtain the bolometric correction with AGN luminosity. They assume a varying relation between optical/UV and X-ray luminosity, which is called a luminosity-dependent bolometric correction. This gives a larger bolometric correction than the constant one at the higher AGN luminosity end, which would make average $L_{bol}^{(AGN)}$ larger and C_T smaller.

The right panel of Figure 14 shows the same plot as Figure 8, but using the luminosity-dependent bolometric correction of Marconi et al. (2004). As expected from the luminosity-dependent bolometric correction, the distribution is slightly shifted to the right and downward in the figure. Actually, the median values of AGN bolometric luminosity and $C_T(\text{dust})$ change from $(\log L_{bol}^{(AGN)}, C_T(\text{dust})) = (44.65, 0.46)$ to $(\log L_{bol}^{(AGN; M04)}, C_T(\text{dust})) = (44.79, 0.39)$.

The figure clearly retains the trend of $C_T(\text{gas} + \text{dust}) \geq C_T(\text{dust})$ over the entire AGN luminosity range. On the other hand, the slight decline in $C_T(\text{dust})$ in the lowest AGN bolometric luminosity bin disappears in Figure 14. This is mainly because of the small statistics in the lowest luminosity bin and some sources being shifted into a higher luminosity bin because of the larger bolometric correction by Marconi et al. (2004).

C.3. Dependence of Additional Torus Parameters

We here discuss how the dust covering factor changes when we change the set of the torus parameters. In this study we have only considered the spectral power-law index (α_1) at $\lambda < 19 \mu$ m for the high-luminosity end with $\log L_{14-150} > 44$, and not considered the dust extinction for obscured AGNs, which could be one of the most significant parameters shaping the torus SEDs. The left panel of Figure 15 shows $C_T(\text{dust})$ as a function of $L_{bol}^{(AGN)}$ after addition of the dust extinction for obscured AGNs using the absorption profile of Draine (2003) (see also Mullaney et al. 2011). $C_T(\text{dust})$ becomes slightly larger, but the overall sense does not change. The middle panel shows the same plot using a fixed power-law index $\alpha_1 = 1.8$ for all sources without the dust extinction. $C_T(\text{dust})$ shows a flatter distribution than Figure 8, but the overall trend of $C_T(\text{dust}) < C_T(\text{gas} + \text{dust})$ still holds.

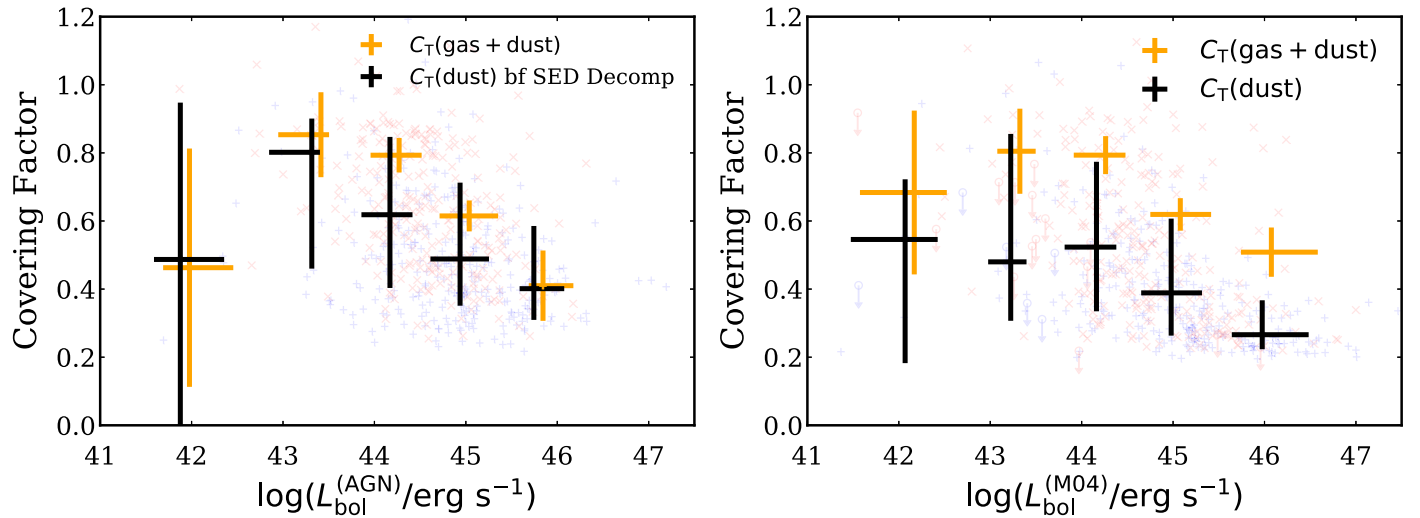


Figure 14. Same as Figure 8, but estimating the values differently. Left: the covering factors used here are based on the estimation using the observed $12\ \mu\text{m}$ luminosities in Ichikawa et al. (2017) before the IR SED decomposition. Right: the bolometric corrections used are dependent on the bolometric luminosity ($L_{\text{bol}}^{(\text{M04})}$; Marconi et al. 2004), not the constant bolometric correction.

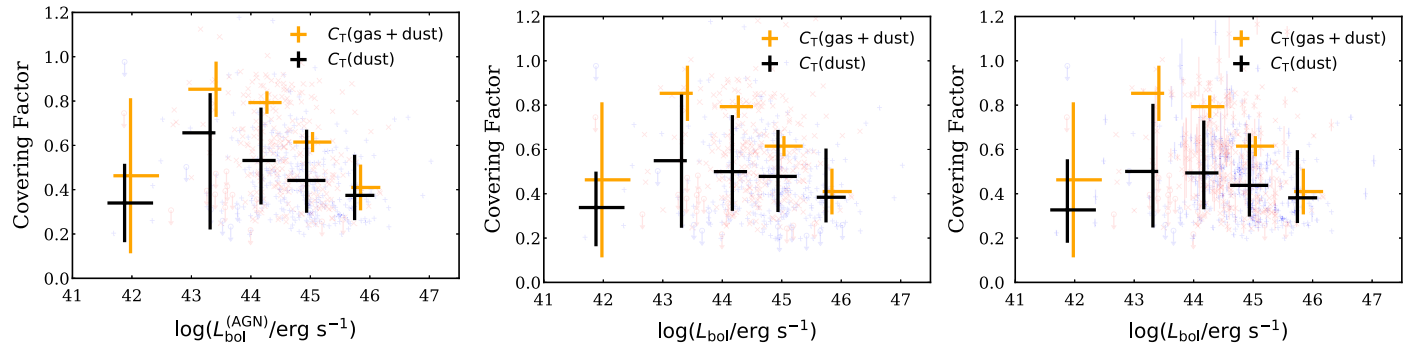


Figure 15. Same as Figure 8, but using a different set of free parameters for (left) the addition of dust extinction and (middle) a fixed power-law index $\alpha_1 = 1.8$. Right: same as Figure 8, but using the averaged $C_T(\text{dust})$ of the SB templates as discussed in Appendix C.4.

C.4. Dependence of Other SB Templates

In this study, we used the best SB template based on the lowest χ^2 value as discussed in Section 3. However, other SB templates sometimes show fitting results of similar quality with small $\Delta\chi^2$ between the best one and the others. Therefore, we investigate here how the result could be affected by using such different SB templates. We consider here that the fitting result is indistinguishable if $\Delta\chi^2$ between the best fitting SB template and the other SB ones is smaller than χ_{max}^2 , which is the maximum allowed χ^2 corresponding to a p -value of $p = 0.05$ of χ^2 distributions with the degree of freedom for each source. If one source has ≥ 2 indistinguishable SB templates, we then measure the averaged $C_T(\text{dust})$ and the standard deviation $\Delta C_T(\text{dust})$. The right panel of Figure 15 shows the result using the averaged $C_T(\text{dust})$ here, and the binned values of $C_T(\text{dust})$ become slightly smaller than the original ones.

ORCID iDs

Kohei Ichikawa <https://orcid.org/0000-0002-4377-903X>
 Claudio Ricci <https://orcid.org/0000-0001-5231-2645>
 Yoshihiro Ueda <https://orcid.org/0000-0001-7821-6715>
 Franz E. Bauer <https://orcid.org/0000-0002-8686-8737>
 Taiki Kawamuro <https://orcid.org/0000-0002-6808-2052>
 Michael J. Koss <https://orcid.org/0000-0002-7998-9581>

Kyuseok Oh <https://orcid.org/0000-0002-5037-951X>
 David J. Rosario <https://orcid.org/0000-0002-0001-3587>
 T. Taro Shimizu <https://orcid.org/0000-0002-2125-4670>
 Marko Stalevski <https://orcid.org/0000-0001-5146-8330>
 Benny Trakhtenbrot <https://orcid.org/0000-0002-3683-7297>

References

- Alexander, D. M., & Hickox, R. C. 2012, *NewAR*, **56**, 93
- Alonso-Herrero, A., Esquej, P., Roche, P. F., et al. 2016, *MNRAS*, **455**, 563
- Alonso-Herrero, A., Pereira-Santaella, M., Rieke, G. H., & Rigopoulou, D. 2012, *ApJ*, **744**, 2
- Alonso-Herrero, A., Ramos Almeida, C., Esquej, P., et al. 2014, *MNRAS*, **443**, 2766
- Alonso-Herrero, A., Ramos Almeida, C., Mason, R., et al. 2011, *ApJ*, **736**, 82
- Asmus, D., Gandhi, P., Hönig, S. F., Smette, A., & Duschl, W. J. 2015, *MNRAS*, **454**, 766
- Asmus, D., Gandhi, P., Smette, A., Hönig, S. F., & Duschl, W. J. 2011, *A&A*, **536**, A36
- Asmus, D., Hönig, S. F., & Gandhi, P. 2016, *ApJ*, **822**, 109
- Asmus, D., Hönig, S. F., Gandhi, P., Smette, A., & Duschl, W. J. 2014, *MNRAS*, **439**, 1648
- Baumgartner, W. H., Tueller, J., Markwardt, C. B., et al. 2013, *ApJS*, **207**, 19
- Beckmann, V., Soldi, S., Ricci, C., et al. 2009, *A&A*, **505**, 417
- Beichman, C. A., Neugebauer, G., Habing, H. J., Clegg, P. E., & Chester, T. J. 1988, *Infrared Astronomical Satellite (IRAS) Catalogs and Atlases. Vol. 1: Explanatory Supplement*
- Brandl, B. R., Agócs, T., Aitink-Kroes, G., et al. 2016, *Proc. SPIE*, **9908**, 990820
- Brandl, B. R., Bernard-Salas, J., Spoon, H. W. W., et al. 2006, *ApJ*, **653**, 1129
- Burtscher, L., Hönig, S., Jaffe, W., et al. 2016, *Proc. SPIE*, **9907**, 99070R

- Burtscher, L., Meisenheimer, K., Tristram, K. R. W., et al. 2013, *A&A*, **558**, A149
- Casey, C. M. 2012, *MNRAS*, **425**, 3094
- Chary, R., & Elbaz, D. 2001, *ApJ*, **556**, 562
- Colina, L., Gonzalez Delgado, R., Mas-Hesse, J. M., & Leitherer, C. 2002, *ApJ*, **579**, 545
- Comastri, A., Gilli, R., Marconi, A., Risaliti, G., & Salvati, M. 2015, *A&A*, **574**, L10
- Cutri, R. M., Wright, E. L., Conrow, T., et al. 2013, in Explanatory Supplement to the AllWISE Data Release Products, ed. R. M. Cutri et al.
- da Cunha, E., Charlot, S., & Elbaz, D. 2008, *MNRAS*, **388**, 1595
- Dale, D. A., Helou, G., Contursi, A., Silbermann, N. A., & Kolhatkar, S. 2001, *ApJ*, **549**, 215
- Davies, R. I., Burtscher, L., Rosario, D., et al. 2015, *ApJ*, **806**, 127
- Del Moro, A., Alexander, D. M., Mullaney, J. R., et al. 2013, *A&A*, **549**, A59
- Delvecchio, I., Gruppioni, C., Pozzi, F., et al. 2014, *MNRAS*, **439**, 2736
- Draine, B. T. 2003, *ARA&A*, **41**, 241
- Elitzur, M. 2012, *ApJL*, **747**, L33
- Esquej, P., Alonso-Herrero, A., González-Martín, O., et al. 2014, *ApJ*, **780**, 86
- Feigelson, E. D., & Nelson, P. I. 1985, *ApJ*, **293**, 192
- Fuller, L., Lopez-Rodriguez, E., Packham, C., et al. 2016, *MNRAS*, **462**, 2618
- Gandhi, P., Hönig, S. F., & Kishimoto, M. 2015, *ApJ*, **812**, 113
- Gandhi, P., Horst, H., Smette, A., et al. 2009, *A&A*, **502**, 457
- García-González, J., Alonso-Herrero, A., Hernán-Caballero, A., et al. 2016a, *MNRAS*, **458**, 4512
- García-Burillo, S., Combes, F., Ramos Almeida, C., et al. 2016, *ApJL*, **823**, L12
- García-González, J., Alonso-Herrero, A., Hernán-Caballero, A., et al. 2016b, *MNRAS*, **458**, 4512
- González-Martín, O., Masegosa, J., Hernán-Caballero, A., et al. 2017, *ApJ*, **841**, 37
- González-Martín, O., Rodríguez-Espinosa, J. M., Díaz-Santos, T., et al. 2013, *A&A*, **553**, A35
- Griffin, M. J., Abergel, A., Abreu, A., et al. 2010, *A&A*, **518**, L3
- Hatziminaoglou, E., Fritz, J., Franceschini, A., et al. 2008, *MNRAS*, **386**, 1252
- Hernán-Caballero, A., Alonso-Herrero, A., Hatziminaoglou, E., et al. 2015, *ApJ*, **803**, 109
- Hönig, S. F., Gandhi, P., Asmus, D., et al. 2014, *MNRAS*, **438**, 647
- Hönig, S. F., Kishimoto, M., Antonucci, R., et al. 2012, *ApJ*, **755**, 149
- Hönig, S. F., Kishimoto, M., Gandhi, P., et al. 2010, *A&A*, **515**, A23
- Hönig, S. F., Kishimoto, M., Tristram, K. R. W., et al. 2013, *ApJ*, **771**, 87
- Ichikawa, K., Imanishi, M., Ueda, Y., et al. 2014, *ApJ*, **794**, 139
- Ichikawa, K., & Inayoshi, K. 2017, *ApJL*, **840**, L9
- Ichikawa, K., Packham, C., Ramos Almeida, C., et al. 2015, *ApJ*, **803**, 57
- Ichikawa, K., Ricci, C., Ueda, Y., et al. 2017, *ApJ*, **835**, 74
- Ichikawa, K., Ueda, Y., Terashima, Y., et al. 2012, *ApJ*, **754**, 45
- Imanishi, M., Nakanishi, K., Izumi, T., & Wada, K. 2018, *ApJL*, **853**, L25
- Inayoshi, K., & Haiman, Z. 2016, *ApJ*, **828**, 110
- Isobe, T., Feigelson, E. D., & Nelson, P. I. 1986, *ApJ*, **306**, 490
- Izumi, T., Kohno, K., Fathi, K., et al. 2017, *ApJL*, **845**, L5
- Jaffe, W., Meisenheimer, K., Röttgering, H. J. A., et al. 2004, *Natur*, **429**, 47
- Jun, H. D., Im, M., Lee, H. M., et al. 2015, *ApJ*, **806**, 109
- Kirkpatrick, A., Pope, A., Sajina, A., et al. 2015, *ApJ*, **814**, 9
- Kormendy, J., & Ho, L. C. 2013, *ARA&A*, **51**, 511
- Koss, M., Trakhtenbrot, B., Ricci, C., et al. 2017, *ApJ*, **850**, 74
- Koss, M. J., Assef, R., Baloković, M., et al. 2016, *ApJ*, **825**, 85
- Krabbe, A., Böker, T., & Maiolino, R. 2001, *ApJ*, **557**, 626
- Krolik, J. H., & Begelman, M. C. 1986, *ApJL*, **308**, L55
- Lamperti, I., Koss, M., Trakhtenbrot, B., et al. 2017, *MNRAS*, **467**, 540
- Lani, C., Netzer, H., & Lutz, D. 2017, *MNRAS*, **471**, 59
- Lanz, L., Hickox, R. C., Baloković, M., et al. 2018, arXiv:1811.02570
- Lavalley, M., Isobe, T., & Feigelson, E. 1992, *adass I*, **25**, 245
- Leftley, J. H., Tristram, K. R. W., Hönig, S. F., et al. 2018, *AJ*, **862**, 17
- López-Gonzaga, N., Burtscher, L., Tristram, K. R. W., Meisenheimer, K., & Schartmann, M. 2016, *A&A*, **591**, A47
- López-Rodríguez, E., Alonso-Herrero, A., Díaz-Santos, T., et al. 2018, *MNRAS*, **478**, 2350
- López-Rodríguez, E., Packham, C., Tadhunter, C., et al. 2014, *ApJ*, **793**, 81
- Lusso, E., Hennawi, J. F., Comastri, A., et al. 2013, *ApJ*, **777**, 86
- Lutz, D., Maiolino, R., Spoon, H. W. W., & Moorwood, A. F. M. 2004, *A&A*, **418**, 46
- Lutz, D., Shimizu, T., Davies, R. I., et al. 2018, *A&A*, **609**, 9
- Lyu, J., Rieke, G. H., & Alberts, S. 2016, *ApJ*, **816**, 85
- Lyu, J., & Rieke, G. H. 2017, *ApJ*, **841**, 76
- Lyu, J., Rieke, G. H., & Shi, Y. 2017, *ApJ*, **835**, 257
- Maiolino, R., Risaliti, G., Salvati, M., et al. 2010, *A&A*, **517**, A47
- Maiolino, R., Shemmer, O., Imanishi, M., et al. 2007, *A&A*, **468**, 979
- Marconi, A., Risaliti, G., Gilli, R., et al. 2004, *MNRAS*, **351**, 169
- Markowitz, A. G., Krumpe, M., & Nikutta, R. 2014, *MNRAS*, **439**, 1403
- Martínez-Paredes, M., Aretxaga, I., Alonso-Herrero, A., et al. 2017, *MNRAS*, **468**, 2
- Masini, A., Comastri, A., Baloković, M., et al. 2016, *A&A*, **589**, A59
- Mason, R. E., Lopez-Rodriguez, E., Packham, C., et al. 2012, *AJ*, **144**, 11
- Mateos, S., Carrera, F. J., Alonso-Herrero, A., et al. 2015, *MNRAS*, **449**, 1422
- Mateos, S., Carrera, F. J., Alonso-Herrero, A., et al. 2016, *ApJ*, **819**, 166
- Matsuoka, K., & Woo, J.-H. 2015, *ApJ*, **807**, 28
- McLure, R. J., & Dunlop, J. S. 2004, *MNRAS*, **352**, 1390
- Meléndez, M., Mushotzky, R. F., Shimizu, T. T., Barger, A. J., & Cowie, L. L. 2014, *ApJ*, **794**, 152
- Mineo, S., Gilfanov, M., & Sunyaev, R. 2012, *MNRAS*, **419**, 2095
- Minezaki, T., & Matsushita, K. 2015, *ApJ*, **802**, 98
- Mullaney, J. R., Alexander, D. M., Goulding, A. D., & Hickox, R. C. 2011, *MNRAS*, **414**, 1082
- Müller-Sánchez, F., Prieto, M. A., Mezcuca, M., et al. 2013, *ApJL*, **763**, L1
- Murakami, H., Baba, H., Barthel, P., et al. 2007, *PASJ*, **59**, S369
- Murphy, E. J., Chary, R.-R., Dickinson, M., et al. 2011, *ApJ*, **732**, 126
- Mushotzky, R. F., Shimizu, T. T., Meléndez, M., & Koss, M. 2014, *ApJL*, **781**, L34
- Neškova, M., Sirocky, M. M., Ivezić, Ž., & Elitzur, M. 2008a, *ApJ*, **685**, 147
- Neškova, M., Sirocky, M. M., Nikutta, R., Ivezić, Ž., & Elitzur, M. 2008b, *ApJ*, **685**, 160
- Netzer, H. 1987, *MNRAS*, **225**, 55
- Netzer, H. 2003, *ApJL*, **583**, L5
- Netzer, H. 2015, *ARA&A*, **53**, 365
- Netzer, H., Lani, C., Nordon, R., et al. 2016, *ApJ*, **819**, 123
- Netzer, H., Lutz, D., Schweitzer, M., et al. 2007, *ApJ*, **666**, 806
- Novak, G. S. 2013, arXiv:1310.3833
- Oh, K., Koss, M., Markwardt, C. B., et al. 2018, *ApJS*, **235**, 4
- Packham, C., Radoski, J. T., Roche, P. F., et al. 2005, *ApJL*, **618**, L17
- Poglitsch, A., Waelkens, C., Geis, N., et al. 2010, *A&A*, **518**, L2
- Privon, G. C., Baum, S. A., O'Dea, C. P., et al. 2012, *ApJ*, **747**, 46
- Raban, D., Jaffe, W., Röttgering, H., Meisenheimer, K., & Tristram, K. R. W. 2009, *MNRAS*, **394**, 1325
- Radoski, J. T., Packham, C., Levenson, N. A., et al. 2008, *ApJ*, **681**, 141
- Ramos Almeida, C., Levenson, N. A., Alonso-Herrero, A., et al. 2011, *ApJ*, **731**, 92
- Ramos Almeida, C., Pérez García, A. M., Acosta-Pulido, J. A., & Rodríguez Espinosa, J. M. 2007, *AJ*, **134**, 2006
- Ramos Almeida, C., & Ricci, C. 2017, *NatAs*, **1**, 679
- Ricci, C., Bauer, F. E., Arevalo, P., et al. 2016, *AJ*, **820**, 5
- Ricci, C., Paltani, S., Awaki, H., et al. 2013, *A&A*, **553**, A29
- Ricci, C., Trakhtenbrot, B., Koss, M. J., et al. 2017a, *Natur*, **549**, 488
- Ricci, C., Trakhtenbrot, B., Koss, M. J., et al. 2017b, *ApJS*, **233**, 17
- Ricci, C., Ueda, Y., Koss, M. J., et al. 2015, *ApJL*, **815**, L13
- Richards, G. T., Lacy, M., Storrie-Lombardi, L. J., et al. 2006, *ApJS*, **166**, 470
- Risaliti, G., Elvis, M., Fabbiano, G., et al. 2007, *ApJL*, **659**, L111
- Risaliti, G., Elvis, M., & Gilli, R. 2002, *ApJL*, **566**, L67
- Risaliti, G., Nardini, E., Salvati, M., et al. 2011, *MNRAS*, **410**, 1027
- Rodríguez Espinosa, J. M., Rudy, R. J., & Jones, B. 1987, *ApJ*, **312**, 555
- Rosario, D. J., Burtscher, L., Davies, R. I., et al. 2018, *MNRAS*, **473**, 5658
- Rosario, D. J., Santini, P., Lutz, D., et al. 2012, *A&A*, **545**, A45
- Sajina, A., Yan, L., Armus, L., et al. 2007, *ApJ*, **664**, 713
- Shimizu, T. T., Meléndez, M., Mushotzky, R. F., et al. 2016, *MNRAS*, **456**, 3335
- Shimizu, T. T., Mushotzky, R. F., Meléndez, M., et al. 2017, *MNRAS*, **466**, 3161
- Simpson, C. 2005, *MNRAS*, **360**, 565
- Stalevski, M., Ricci, C., Ueda, Y., et al. 2016, *MNRAS*, **458**, 2288
- Stanley, F., Harrison, C. M., Alexander, D. M., et al. 2015, *MNRAS*, **453**, 591
- Symeonidis, M., Giblin, B. M., Page, M. J., et al. 2016, *MNRAS*, **459**, 257
- Trakhtenbrot, B. 2014, *ApJL*, **789**, L9
- Tran, Q. D., Lutz, D., Genzel, R., et al. 2001, *ApJ*, **552**, 527
- Treister, E., Krolik, J. H., & Dullemond, C. 2008, *ApJ*, **679**, 140
- Tristram, K. R. W., Burtscher, L., Jaffe, W., et al. 2014, *A&A*, **563**, A82
- Tueller, J., Mushotzky, R. F., Barthelmy, S., et al. 2008, *ApJ*, **681**, 113
- Ueda, Y., Akiyama, M., Hasinger, G., Miyaji, T., & Watson, M. G. 2014, *ApJ*, **786**, 104
- Ueda, Y., Akiyama, M., Ohta, K., & Miyaji, T. 2003, *ApJ*, **598**, 886
- Ueda, Y., Hiroi, K., Isobe, N., et al. 2011, *PASJ*, **63**, S937
- Wright, E. L., Eisenhardt, P. R. M., Mainzer, A. K., et al. 2010, *AJ*, **140**, 1868
- Xu, L., Rieke, G. H., Egami, E., et al. 2015, *ApJS*, **219**, 18
- Yu, Q., & Tremaine, S. 2002, *MNRAS*, **335**, 965